The Two Sides of Silicon Detectors

Steven R H Devine

UNIVERSITY
of
GLASGOW

Department of Physics and Astronomy
University of Glasgow

Thesis submitted for the degree of
Doctor of Philosophy

October 2001

©Steven R H Devine.

ProQuest Number: 13818846

All rights reserved

INFORMATION TO ALL USERS
The quality of this reproduction is dependent upon the quality of the copy submitted.

In the unlikely event that the author did not send a complete manuscript
and there are missing pages, these will be noted. Also, if material had to be removed,
a note will indicate the deletion.

ProQuest 13818846

Published by ProQuest LLC (2018). Copyright of the Dissertation is held by the Author.

All rights reserved.
This work is protected against unauthorized copying under Title 17, United States Code
Microform Edition © ProQuest LLC.

ProQuest LLC.
789 East Eisenhower Parkway
P.O. Box 1346
Ann Arbor, MI 48106 – 1346

GLASGOW
UNIVERSITY
LIBRARY:
12496
COPY 1

Even though they have left me behind,

I have not forgotten their inspiration.

Abstract

Results are presented on *in situ* irradiation of silicon detector's at cryogenic temperature. The results show that irradiation at cryogenic temperatures does not detrimentally effect a silicon detectors performance when compared to its irradiation at room temperature. Operation of silicon devices at cryogenic temperatures offers the advantage of reducing radiation-induced leakage current to levels of a few pA, while at 130K the *Lazarus Effect* plays an important role i.e. minimum voltage required for full depletion. Performing voltage scans on a 'standard' silicon pad detector pre- and post annealing, the charge collection efficiency was found to be 60% at 200V and 95% at 200V respectively. Time dependence measurements are presented, showing that for a dose of
6.5×10^{14} p/cm^2 (450GeV protons) the time dependence of the charge collection efficiency is negligible. However, for higher doses, 1.2×10^{15} p/cm^2, the charge collection efficiency drops from an initial measured value of 67% to a stable value of 58% over a period of 15 minutes for reversed biased diodes.

An analysis of the "double junction" effect is also presented. A comparison between the Transient Current Technique and an X-ray technique is presented. The double junction has been observed in $p^+/n/n^+$ silicon de-

tectors after irradiation beyond "type inversion", corresponding to a fluence equivalent to $\sim$3x10^{13}cm^{-2} 1MeV neutrons, producing $p^+/p/n^+$ and essentially two p-n junctions within one device. With increasing bias voltage, as the electric field is extending into the detector bulk from opposite sides of the silicon detector, there are two distinct depletion regions that collect charge signal independently. Summing the signal charge from the two regions, one is able to reconstruct the initial energy of the incident particle. From Transient Current measurements it is apparent that E-field manipulation is possible by excess carrier injection, enabling a high enough E-field to extend across the width of the detector, allowing for efficient charge collection .

Acknowledgements

What a nightmare this thesis has been for everyone who has had to drag me through it! This is my opportunity to thank some of the most influential people who helped me through, not only my thesis but everything the last three years have thrown at me.

Firstly, I would like to thank my supervisor/mentor/father-figure, **Ken**. Truly without his patience and diligence reading over my "journalistic" overtures to this work, I would not have succeeded.

I would also like to thank **Rick**, my second supervisor for his comments and guidance even while he was holding *Countless Difficult Factions* together. Also **Mahfuzur** who earns more and more respect by the breadth of his knowledge. I would also like to thank **Pat Nicholson** for his patience, and maybe one day I *will* finish that experiment!

Many ideas that I have had have come through stimulating discussions with **Steve Watts** and **Cinzia Da Via**. I cannot thank then enough for their generosity and their friendship.

Whenever I would get over enthusiastic about anything, **Val** was always there to *squash* it. Without his sobering counsel and company, this may have indeed been a *flare up point.*

Talking about flaring up...**The-Boy-Passmore**, for just less than three years my office mate, and I could not have asked for better. Later, the addition of **Patrick**, who must have felt like he had entered a gladiatorial arena, only enhanced the atmosphere that I had enjoyed so much.

Just next door, the 329b-boys always offered excellent amusements. **Corporate-Craig**, who knows the virtues of a birch tree, **John "The Simpson's" Watt**, with whom I now re-enact every episode that ever was, and **Keith**, who while being a complete *wideo*, could answer any questions I had about all this. Substituting this year in 329b, are **David** and **Julien**, the former teaching the finer points of squash and golf and the latter...never to own a rabbit! And of course **Pamela**, whose love of chocolate *may* only be surpassed by my own.

Any other time I needed help, I would always ask **Richy**, and he would always have the answer. **Fred, Drew, John, Pamela**, and the late **Frank**, were always more helpful than they needed to be and always an excellent laugh.

Financially I have benefited from the generosity of **PPARC** and also my CASE sponsors, **RAL**. The Physics and Astronomy department and the Royal Society of Edinburgh have contributed financially to workshops and exchanges I have been involved in. As a result I would like to thank **David Saxon**, who is always supportive from his "modestely sized professor's office". On one trip to Vilnius, I had an interesting time, both regarding research and socially. This would not have been possible without **J. Vaitkus, E. Gaubas** and **V. Kazukauskas**. I would like to also thank **K. Pozela** for his hospitality and for the conversations we have had regarding our research.

Without doubt **Catherine** has kept me from trouble more times than I can possibly recall. I owe her so much...

The last three "PhD years" have been shared with **Young John**, and more than once he has pulled me back from the brink...many an evening have we shared with all the above, as well as **Anna, Gavin, Liam, Sinead, Tatjana** and of course **Big Stan** down at Tennents, and the occasional Wednesday *residing at the bar.* If not drinking in Glasgow, we would be drinking in Geneva. While based at CERN, many people contributed to what was a really happy time for me. I would like to mention in particular **Gennaro** who has been a good friend. Working within the *RD39 Mafia* has been an excellent experience for me. Thanks to **Zheng** who showed me warmth in New York while it was snowing outside.

So many friends have been supportive throughout not only my PhD but through everything. Always making me feel that I have been doing something really worthwhile. I want to mention especially **Ewan**, who has taught me the finer points of wine, beer, and whisky. Also, **Derek**, without whose difficult "What is the universe all about?" questions, I may have forgotten why I was doing all this.

My family has, as always, been more supportive than I could have asked for. I regret that there is no way I can get all your names on here! I want to mention especially though the patience of my **Mum** and **Cristina**, thank-you! Thanks also to **Dad**, without whom my car would never run.

Gayle, for whom words would only fail...but I maintain that I was not as *Huffy* as she!!

Declaration

Except where explicit reference is made to the work of others, this dissertation is the result of my own work. None of this material has been submitted for any other degree at the University of Glasgow or any other institute.

Steven Devine

Contents

1 Introduction **2**

2 Detector Theory **8**

2.1 Silicon Device Fabrication 8

2.1.1 Semiconductor Grade Silicon (SGS) 9

2.1.2 Czochralski Silicon (Cz) 10

2.1.3 Float Zone Silicon (FZ) 11

2.2 p-n Junction 13

2.3 Depletion Region 16

2.3.1 Abrupt Junction 16

2.3.2 Bias Voltage 22

2.3.3 Depletion Capacitance 23

2.4 Signal Generation 25

2.4.1 Ramo's Theorem 26

2.4.2 Charge loss 28

2.4.3 Alpha Particles 29

2.4.4 Minimum Ionising Particles (MIPS) 29

2.4.5 X-rays 30

2.4.6 Photoelectric Effect 33

2.4.7 Compton Scattering 34
2.5 Readout 34
2.5.1 The Charge Sensitive Amplifier 35
2.5.2 Pulse Shape 35
2.6 Summary 38

3 Detector Irradiation **39**
3.1 Motivation 39
3.2 Radiation Defects 40
3.3 Preventions and Cures 42
3.3.1 NIEL Scaling Hypothesis 43
3.3.2 Oxygen Enriched Silicon 46
3.3.3 The Lazarus Effect 47
3.3.4 Experimental Set-up 51
3.4 Detecting Defects 54
3.4.1 I-V Measurements - Leakage Current 54
3.4.2 Deep Level Transient Spectroscopy (DLTS) 55
3.4.3 Transient Current Technique (TCT) 60
3.4.4 Microwave Absorption (MWA) 62
3.5 Summary 70

4 Double Junction in Irradiated Silicon **72**
4.1 *In Situ* Irradiation of Cryogenic Silicon 72
4.1.1 Experimental Set-up 73
4.1.2 Temperature Scan Results 74
4.1.3 Interpretation of the Results 75

4.2 The Double Junction 76
4.2.1 Experimental Set-up 77
4.2.2 Calibration 78
4.2.3 Sample Preparation 79
4.2.4 Analysis 80
4.2.5 Voltage Scans 82
4.2.6 Temperature Scans 86
4.2.7 Count Rate 88
4.2.8 Discussion 90

5 Discussions **93**

5.1 Conclusions and Future Experiments 93

List of Figures

1.1 A Higgs candidate seen by ALEPH at LEP, CERN. 4

2.1 Schematic of the Czochralski crystal puller. 11

2.2 Schematic of the Float Zone growth method. 12

2.3 Electric field in the depletion region of a p-n junction 14

2.4 Schematic of the doping profile of an abrupt junction. 17

2.5 (a) Space charge distribution in the depleted region at thermal equilibrium. (b) Schematic of E-field distribution. The area under the graph represents the built-in potential. 18

2.6 A schematic representation of (a) a one-sided abrupt junction with $N_A >> N_D$ (b) Space charge distribution (c) Electric-field distribution (d) Potential variation with distance, x. 21

2.7 Schematic representation of depletion layer width and band bending of a p-n junction under (a) equilibrium conditions (b) forward bias and (c) reverse bias conditions. 23

2.8 Energy loss rate in silicon for different high energy particles [22]. 31

2.9 Graph of the variation of photon interaction cross-sections with photon energy. [23] 32

2.10 Schematic representation of the photoelectric effect. 33

2.11 Schematic representation of the Compton effect. 34
2.12 Expected charge pulse shapes in an ideal detector of planar geometry for (a) an interaction in the central region and (b) an interaction near one of the collection electrodes. 36
2.13 Simplest equivalent circuit of detector with planar geometry. The ohmic resistance of the reverse biased junction is not shown here due to its very high value. 37

3.1 Schematic of irradiated silicon lattice. 40
3.2 Schematic of some of the radiation-induced trap levels in the silicon energy band.[26] 41
3.3 Displacement damage function, D(E), in silicon showing the "hardness factor" values one may use to normalise radiation dose for pions, protons and electrons to that for 1MeV neutrons [30][31][32][33][34]. 44
3.4 Comparison of standard float zone silicon and oxygen enriched silicon when irradiated with protons, pions, and neutrons [10]. 48
3.5 Graph showing various measurements made in irradiated devices [43]. The maximum CCE occurs at around 130K in all bias voltage cases, irrespective of the dose. 51
3.6 The image on the right is the cryostat used in the CERN SPS test beam area to irradiate silicon diodes held at near liquid nitrogen temperature. The left schematic shows the set-up inside the cryostat and also the trigger scintillation counters. . 53

3.7 DLTS process showing initial forward bias pulse, then returning to negative bias and the corresponding capacitance transient [45]. 57
3.8 DLT spectra measured on a non-irradiated diode at different injection pulse duration and corresponding "lock-in" frequencies. 58
3.9 DLT spectra measured on the Pb-ion irradiated sample S7 and compared with unirradiated sample S21. 59
3.10 DLTS comparison [46]. for different irradiation sources. 60
3.11 Sample A (SA) illuminated from p-side, electron drift 62
3.12 Sample B (SB) illuminated from n-side, hole drift. 63
3.13 Sample C (SC) illuminated from the p-side. 64
3.14 Sample D (SD) illuminated from the p-side. 65
3.15 Sample E (SE) illumination from p-side. 66
3.16 Sample F (SF) illuminated from p-side. 67
3.17 Schematic representation of the MWA technique experimental set-up showing a diode under illumination. 67
3.18 Excess carrier decay kinetics obtained on both irradiated and non-irradiated samples. Samples S21–S27 are non-irradiated diodes, while the others have various dose levels as documented in Table 3.2. 68

4.1 Graphs of the CCE.(a) Calibration curve with non-irradiated device and heavily irradiated device showing the CCE before annealing for 1 hour at 207K. (b) The CCE of the heavily irradiated sample taken as temperature is increased. (c) Comparison of the CCE of the heavily irradiated sample before and after warming. (d) Time dependence of the CCE is shown to be connected to the dose of irradiation. 75

4.2 Schematic diagram of the cold finger cryostat used at Brunel to obtain results with X-ray sources on silicon devices. 77

4.3 Graph showing Counts per channel vs. MCA Channel Number. Each channel corresponds to a particular energy, defined by the characteristic photo peak of each source. 79

4.4 Graph showing penetration of 60keV X-rays into silicon. This was performed using Photcof (a 2D detector simulation software package). 81

4.5 Possible X-ray interactions. (a) Photon interaction at the front depleted layer will give a signal contribution from the high E-field region. (b) In the "dead" low E-field region one assumes no, or very little, contribution to the collected signal charge. (c) Interaction in the back depleted region will also give a signal charge contribution due to the e-h movement in the high E-field. 83

4.6 Multi-channel analyser data for temperature scans at 80V. Peak 1 corresponds to the electric field region near the P^+ contact. It is at a lower position, corresponding to less collected signal charge. Peak 2 corresponds to the higher position and higher collected charge peak. The signal collected is from the region near the n^+ contact with its higher electric field. . . . 85

4.7 Multi-channel analyser data for temperature scans at 80V. . . 87

4.8 Depletion width sizes estimated from photo peak count rates. 89

4.9 Measurements made at BNL. 91

List of Tables

2.1 Photon Intensities per Disintegration of ^{241}Am 32

3.1 Comparisons of trapping (subscript n denotes electron values) and de-trapping (subscript p denotes hole values) times of relevant defects as a function of the position in the bandgap.[38][39][40]. 49

3.2 Irradiation fluence and carrier lifetime for each sample measured. 69

4.1 Energies emitted from sources used for calibration 78

Chapter 1

Introduction

Detection of radiation was accidental when, in 1896, Becquerel placed uranium salt over photographic film and, when the film was developed, it had been "fogged" by the ionising particles released from the uranium [1].

Since the discovey of ionising radiation, the development of radiation detectors in the major classes, visual and electronic, has evolved substantially. In the former, film, cloud and bubble chambers as well as higher trigger rate spark and streamer chambers, create a visual record of the trajectory of an ionising particle via developed emulsion grains, condensation droplets in a supersaturated vapour, bubbles in a superheated liquid or electrical discharges, respectively, located on the ion trail created in the medium by the ionising radiation. The performance limitations in the operating rate of these devices and the analysis of the photographic images [2] used for event storage, together with the advent of colliding beam accelerators, have led to their large scale replacement by electronic detectors. Electronic detectors have evolved similarly, from the gold-leaf electroscopes, used in early investigations of cosmic rays, to ionisation chambers, Geiger tubes and proportional

and streamer chambers. In scintillation counters, short low intensity light pulses from phosphors, converted to electrical pulses using phototubes, have provided the backbone of the majority of High Energy Physics (HEP) accelerator experiments for several decades. More recently (circa 1980), semiconductor detectors have been used as a replacement for particle tracking devices [3].

Semiconductor detectors behave like solid state ionisation chambers. Incident particles deposit ionisation energy, producing electron hole pairs in the material which separate due to the presence of an applied electric field. The charge signal is collected at the electrodes and is proportional to the deposited energy. Semiconductor detectors offer excellent energy and spatial resolution (pixel sizes $<1\text{mm}^2$) for particle identification. Particle decay vertices very close to the interaction point of the colliding beams need to be resolved from the primary interaction point as the lifetimes of the particles created are very short, (typically 10^{-12}s to 10^{-13}s). Figure 1.1 [4] shows the importance of the precision tracking (few μm) of the inner silicon layers of a collider vertex detector, without which this event would probably not have been detected. Of course the closer that one places the device to the beam cross-over point, the higher the flux of particles bombarding the detector, the higher the level of radiation damage to the detector medium and read-out electronics will be, limiting typical silicon detector lifetimes to particle fluences of about $\leq 10^{14}\text{cm}^{-2}$ 1MeV equivalent neutrons (c.f. Section 3.3.1). It is of paramount importance to increase the tolerance of semiconductor detectors to harsh radiation environments as the replacement costs are high. Combatting the radiation-induced degradation of signal is extremely impor-

tant, especially for the harsh radiation environments expected at the Large Hadron Collider (LHC), CERN. Currently the LHC switch-on, expected in 2005, will require greater radiation resistant detectors than any of its predecessors. The LHC machine will provide proton-proton collisions at a centre of mass energy of 14TeV with design luminosity of $10^{34}cm^{-2}s^{-1}$, testing the Standard Model and looking for physics beyond it, such as supersymmetric particles. As well as this it will provide heavy ion Pb-Pb collisions. Four experimental collaborations are pro-active for LHC physics: two general purpose detectors, ATLAS and CMS, plus two more specialised detectors, LHCb and ALICE, looking at b-physics and heavy ion physics respectively.

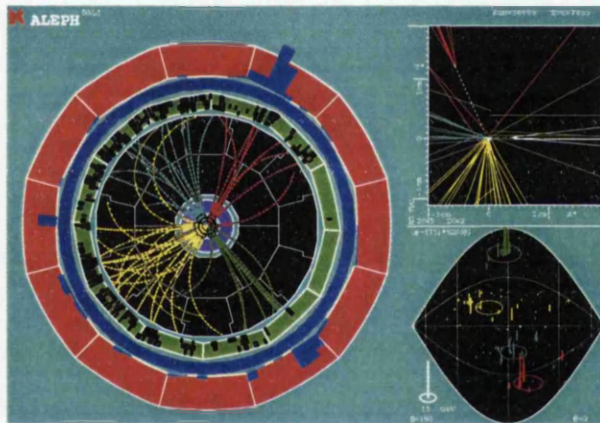

Figure 1.1: A Higgs candidate seen by ALEPH at LEP, CERN.

The pixel detector of the ATLAS[1] experiment will receive a radiation dose of $5x10^{14}$ 1MeV equivalent neutrons cm^{-2} [5] over ten years of operation, more than any previous silicon detector device could withstand. This will be the harshest high energy particle accelerator radiation environment to-date and as such offers a tremendous challenge for device physicists to en-

[1] A Large Toroidal ApparatuS.

sure detector reliability throughout the scheduled 10-year lifetime of ATLAS. Working to meet these challenges, CERN is involved in several Research and Development (RD) programmes with international groups of scientists and universities whose aim is to improve the radiation hardness of silicon. RD48, the ROSE Collaboration, in particular has been extremely successful in meeting these challenges through stringent defect analysis and defect engineering [6]. By identification of the energy levels of defects and charge carrier trapping characteristics, the Collaboration has been able to neutralise some of the radiation-induced damage by the introduction of additional oxygen at the wafer growth stage.

As well as microscopic enhancements to semiconductor detectors, one may also make macroscopic changes to improve performance. The RD39 Collaboration is working towards radiation hard detectors by operation at cryogenic temperatures. The improvement of highly-irradiated silicon detectors when operated at liquid nitrogen temperature (77K) was first realised by Cinzia Da Via and Vittorio Palmieri in 1998 [7]. Placing a heavily irradiated silicon device, essentially "dead", into liquid nitrogen, they found that one could again detect charge: in essence the detector appeared to them to have come back to life, hence the name: The Lazarus Effect. From this, the RD39 Collaboration was conceived with the following goals:

1) Demonstrate that irradiation during operation at low temperatures does not affect the results obtained with detectors irradiated at room temperature and so concentrate on materials that could reduce detector cost .

2) Demonstrate successful operation of radiation hard CMOS chips operation at Liquid Nitrogen (LN_2) temperatures.

3) Demonstrate that low mass cooling at LN_2 is feasible at a reasonable cost and that electrical and optical feed-through problems of a large system may be mastered.

Goal 1 is dealt with in detail in Chapter 4, while Goals 2 and 3 are work in progress within the RD39 Collaboration at CERN [8]. The concept of the low mass cooling system is to determine whether cryogenic operation of semiconductor detectors is a feasible option for large particle detectors where it is imperative to minimise the scattering and gamma conversion in tracking detector material for accurate track reconstruction. The ATLAS experiment will benefit greatly from input from both RD48 and RD39. This thesis focuses in particular on the behaviour of irradiated silicon detectors at a macroscopic level, addressing how defects occur, how they may be detected, and how they may be neutralised. Chapter 2 details the beginning of a silicon detector's life by describing how silicon wafers are grown and then processed. The chapter continues by detailing how signal is created in the device by different types of ionising radiation. This ionising radiation inflicts damage to the silicon lattice and it is important that one can identify this damage. Chapter 3 deals with the material characterisation processes and outlines different yet complementary techniques. With these tools in place it is then possible to make measurements. Goal 1 from the RD39 Collaboration guidelines is realised in Chapter 4. Results are presented of irradiation of cryogenic silicon with 450GeV protons at the CERN-SPS facility. This result allows a direct comparison to room temperature irradiation, and proves that irradiation in the cold delivers no adverse effects but can only improve detector behaviour. From irradiation tests performed by the RD39 Collabo-

ration it became clear that an interesting phenomenon was occurring inside the p-n junction detector. Further research showed that other groups had also noted similar behaviour. While initially the effect was documented in 1963 by Dearnaley [9], it was put into context by Alexander Chilingarov of the Lancaster group, also working under the umbrella of the ROSE Collaboration. He found that an irradiated detector will in fact have two high field regions, one at each contact, connected via a low central field. This will occur after type inversion of the bulk through irradiation. The detectors used in this thesis are all initially $p^+/n/n^+$, and with a dose beyond $\sim$ 1x10$^{13}/cm^2$ 1MeV equivalent neutrons, the bulk changes from n-type to p-type through the change of space charge, N_{eff}. This gives rise to two p-n junctions as even though the bulk will remain less "positive" than the p^+ contact, it will be more "positive" than the n^+ contact ($p^+/p/n^+$), causing the so-called "double junction" effect. This is examined by a technique pioneered by Steve Watts and Cinzia Da Via at Brunel University who are also members or the RD48 and RD39 Collaborations. Using X-rays to analyse the silicon bulk, one can make spectroscopic measurements from which to infer the depletion zone sizes, due to the nature of the X-ray interactions within the silicon bulk. This chapter closes with a discussion and comparison with results obtained using the Transient Current Technique, pioneered by V. Eremin. The thesis is brought to a close with Chapter 5 which contains final discussions and options for the future. Details are given of how the characterisation process may be improved and where detectors will need to be positioned for possible future upgrades to the LHC.

Chapter 2

Detector Theory

This chapter provides an overview of the basic semiconductor theory that has been used to analyse and test the devices that are reported in subsequent chapters. It is useful to have an idea of the fabrication techniques for a diode detector and how the processes influence the behaviour of a device. In particular, the influence of low concentrations of impurity atoms (such as oxygen), introduced during crystal growth, has been shown to be an important consideration in studies of radiation hardness enhancement by "defect engineering" [10]. Knowing what is expected from a detector, and how the charge generated in the active area of the device is interpreted as signal is of paramount importance as the results presented later rely heavily on the ideas in this chapter.

2.1 Silicon Device Fabrication

Several techniques for silicon crystal growth are outlined in the following sections. The work reported in this thesis was performed entirely on Float Zone

silicon and for this reason it will be given more emphasis. Detector grade silicon must be optimised for two important criteria: very high resistivity ($> 1k\Omega cm$) and high minority carrier lifetime with low bulk generation current. The former is required to enable full depletion of a detector of $\sim 200\mu m$ to $300\mu m$ thickness at a reasonable bias voltage ($\leq$100V), while the latter helps to minimise detector noise. Float zone material meets these needs with the highest purity and hence is used for most detector applications.

2.1.1 Semiconductor Grade Silicon (SGS)

A silicon detector starts off its life as very pure sand. At this point the impurities present are Al_2O_3 and Fe_2O_3 (in the order of a few tenths of a percent). The silicon dioxide is melted down with coke and wood chips in an electrode furnace at around 1780°C. The main chemical reaction that takes place is:

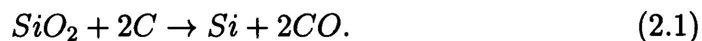

$$SiO_2 + 2C \rightarrow Si + 2CO. \qquad (2.1)$$

The silicon liquid is 99% pure at this point. When this liquid cools it forms a solid that is known as metallurgical grade silicon (MGS). By grinding this into a fine powder and heating to 300°C in HCl gas, causing the chemical reaction:

$$Si + 3HCl \rightarrow SiHCl_3 + H_2 \qquad (2.2)$$

trichlorsilane and hydrogen are produced. Trichlorsilane has a very low boiling point, 31.7°C, while many impurities have a much higher boiling point, so that by distillation the impurity concentration may be reduced below 1 ppb. The trichlorsilane is passed with hydrogen over a silicon rod kept at ~900°C so that the above reaction is reversed with a deposition rate of polysilicon of less than 1mm/h.

2.1.2 Czochralski Silicon (Cz)

For micro-electronics, the purity of the silicon is not as important as it is for semiconductor detectors. As a consequence of this, the majority of commercially grown silicon is Czochralski silicon. This is fast and cheap to produce while still maintaining high resistivity. Named after J. Czochralski, the process involves "pulling" the silicon crystal from a melt, as shown in Fig. 2.1.

High purity polysilicon, obtained as described in Section 2.1.1, is melted with additional dopants, required to ensure a pre-defined resistivity, in a rotating quartz crucible. A single crystal silicon seed is placed on the surface, and while rotating, is drawn upward. The molten silicon solidifies and extends from the seed as a continuous crystal. During the process of "seed-pulling" the crucible dissolves partially, releasing oxygen into the melt. Over 99% is lost through evaporation from the molten surface, but the remainder dissolves into the single crystal silicon. Oxygen is always the impurity with the highest concentration in Cz silicon, with typical values of 5 to $10 \times 10^{17} cm^{-3}$. This does offer some advantages, as will be discussed in more detail in Chapter 5. The oxygen allows internal gettering, making the silicon crystal more resilient to thermal stress, and more appealing for integrated

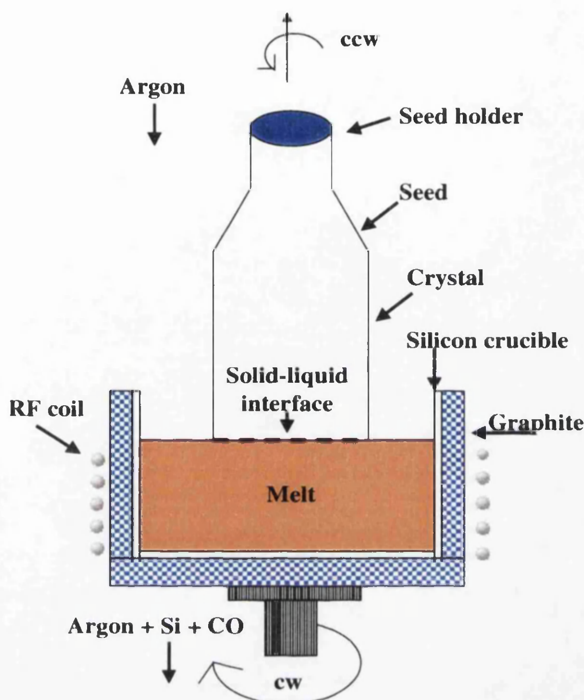

Figure 2.1: Schematic of the Czochralski crystal puller.

circuit production.

2.1.3 Float Zone Silicon (FZ)

The FZ method is shown pictorially in Fig. 2.2.

The production takes place under vacuum or in an inert gaseous atmosphere. A high-purity crystalline rod and a crystal seed are held together in vertical position and rotated. Partial melting is accomplished by a radio frequency field. Drops of the melt are formed on the tip of the polycrystalline rod and the seed is raised to make contact. The diameter is allowed to increase and tapers to a desired diameter for steady-state growth. The molten

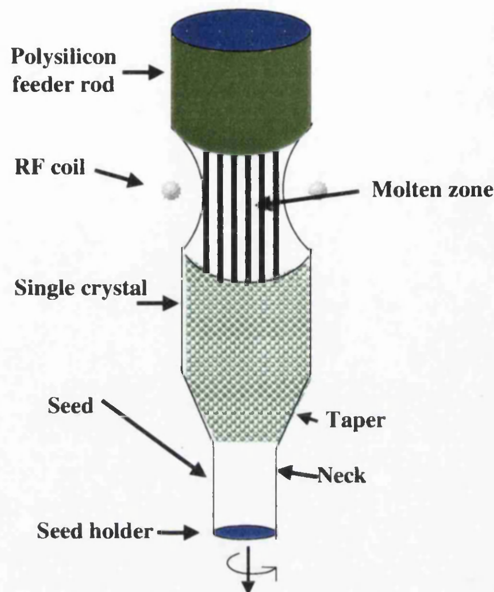

Figure 2.2: Schematic of the Float Zone growth method.

zone moves along the polysilicon rod and solidifies into a single crystal while the material is simultaneously purified. Typical oxygen concentration in FZ silicon is below $5\text{x}10^{15}\text{cm}^{-3}$. For production of p-type silicon one adds diborane (B_2H_6) and to produce n-type one dopes with phosphine (PH_3). The molten silicon is only in contact with the ambient gas, which may also be used to dope the material so that no additional impurities will permeate the silicon. P-type material is easier to produce due to the segregation of the boron atoms.

Neutron Transmutation Doping (NTD)

Float Zone material displays dopant micro inhomogeneity from temperature fluctuations, melting phenomena and dopant segregation due to the material's lack of symmetry. If one also considers the fact that n-type silicon is less

homogeneous than p-type then an interesting solution presents itself in the form of NTD. For NTD, a high purity p-type FZ ingot is subject to neutron bombardment in a reactor. This produces unstable ^{31}Si, which decays with a half-life of 2.62 hours into stable ^{31}P. The neutrons can penetrate ~100cm and so dope the material uniformly but they also introduce radiation damage. These defects are annealed at 800°C, where the phosphorus dopant activates, altering the material to become high resistivity n-type silicon material.

2.2 p-n Junction

The main work of this thesis was carried out on p-n junction diode detectors. Both p-type and n-type regions can be doped into a grown substrate as described above. This structure behaves as a diode rectifier in that it conducts primarily in one direction. Current-Voltage characteristics, described in detail in Section 4.1, show that the properties of the p-n junction are similar to those of an ideal diode. For silicon doped with donors, the material will be n-type, with predominantly electron charge carriers and with the Fermi level nearer the conduction band. Doping with acceptors gives p-type, with predominantly hole charge carriers, and the Fermi level lies nearer the valence band. The junction is formed when these two regions are combined during fabrication by means of epitaxy, diffusion or ion implantation. When the two regions come into contact, diffusion of the carriers occurs. Holes from the p-side diffuse into the n-side and electrons from the n-side diffuse into the p-side. As the holes move into the n-side, they leave behind un-compensated negative acceptor ions, with concentration N_A, near the junction, giving it a negative charge. When electrons diffuse into the p-side, positive donor ions,

with concentration N_D, are left behind, leaving the boundary with a positive charge. At the boundary the excess negative space charge in the p-side and excess positive space charge in the n-side creates an electric field in the direction from the n-side to the p-side, as shown in Fig. 2.3. The E-Field is in the opposite direction to the diffusion current for each type of carrier. As the electrons diffuse from the n-side to the p-side and the field is also from the n-side to the p-side, the net current flow is zero for electrons in equilibrium. A similar situation occurs for holes. The holes diffuse from the p-side to the n-side, the opposite direction of the E-field. The result is no net current in equilibrium.
This may be formalised as:

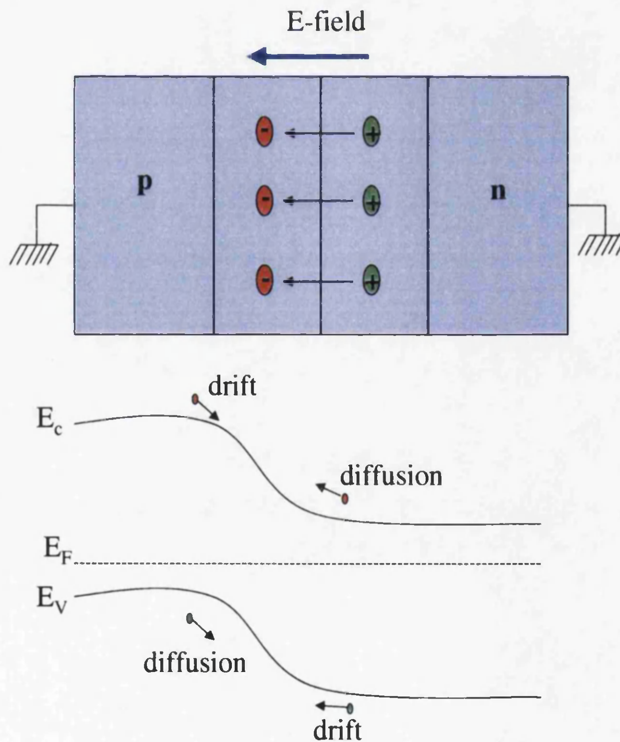

Figure 2.3: Electric field in the depletion region of a p-n junction

$$J_p = J_p(drift) + J_p(diffusion) \qquad (2.3)$$
$$= q\mu_p p E - qD_p\left(\frac{dp}{dx}\right)$$

where the subscript p denotes the value for holes, J is the current density, q the charge, μ the mobility and p the hole concentration, E the electric field, and D the diffusion constant. The derivative term is the rate of change of hole concentration over detector thickness, x. A similar expression exists for electrons. From the Einstein relation one may substitute $D_p=kT\mu_p/q$, and also the expression for the hole concentration:

$$p = n_i e^{(E_i - E_F)/kT} \qquad (2.4)$$

where n_i is the intrinsic carrier concentration. Substitution into Equation 2.4 yields the result that the net hole current density must be zero. The same is true for the electron current density. For the condition of zero net current to be satisfied, the Fermi level must be constant across the bandgap (Fig. 2.3). Placing a neutral region between the p and n regions induces a small transition region from the junction to that region. The space charge of the impurity atoms is compensated by the mobile carriers. The mobile carrier density inside the neutral region is zero. Beyond the transition region is the depletion region, also known as the space charge region. In typical silicon detector diodes, the width of the depletion region compared to the size of the transition region is very large. The typical cases reported here have depletion

widths of 300 to 400μm, whereas the transition region is of the order of a few nanometres. For this reason the transition region is neglected and the depletion region of a fully depleted detector is synonymous with the physical width of the device.

2.3 Depletion Region

The neutral charge region is the active region of the semiconductor device. In this region p=n=0. One then has Poisson's equation in the form:

$$\frac{d^2\psi}{dx^2} = \frac{q}{\epsilon_s}(N_A - N_D) \tag{2.5}$$

where ψ is the electrostatic potential, ϵ_s is the permittivity and N_A and N_D have the same meanings as defined earlier. In order to solve this equation one must know the impurity concentrations. Impurities may be introduced by shallow diffusion or by low-energy ion implantation. An example of such doping is the abrupt p-n junction diode. One may approximate this as in Fig. 2.4.

The next section deals with the abrupt junction and formalises the idea of the depletion region, the "active" part of a diode detector.

2.3.1 Abrupt Junction

In order to analyse the abrupt junction one must consider Poisson's equation, Equation 2.5. As the space charge is distributed non-linearly through the junction, Fig. 2.5(a), one must invoke boundary conditions for a solution.

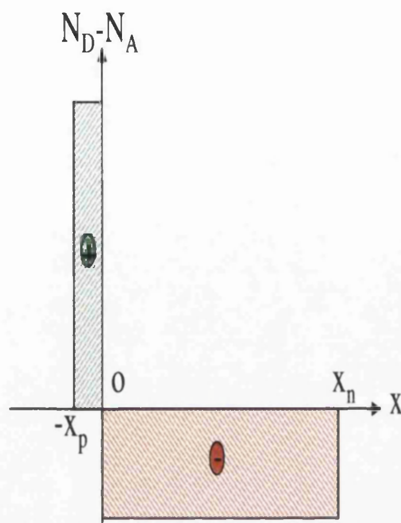

Figure 2.4: Schematic of the doping profile of an abrupt junction.

In the depletion region, Fig. 2.5(a), free carriers are totally depleted so that Equation 2.5 may be simplified to:

$$\frac{d^2\psi}{dx^2} = \frac{+q}{\epsilon_s}(N_A) \text{ for } -x_p \leq x \leq 0 \tag{2.6}$$

and

$$\frac{d^2\psi}{dx^2} = \frac{-q}{\epsilon_s}(N_D) \text{ for } 0 \leq x \leq x_n \tag{2.7}$$

The detector has neutral overall charge, so that the negative space charge density per unit area in the p-side must cancel the positive space charge density per unit area of the n-side:

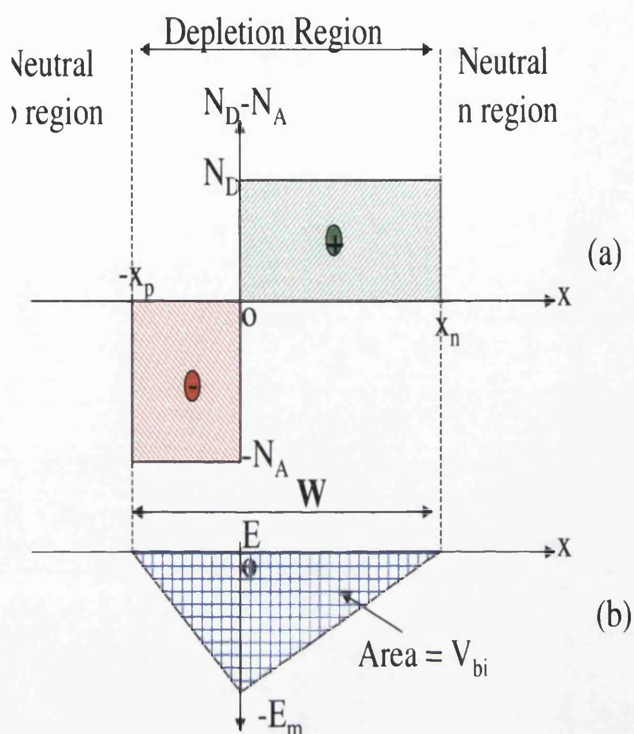

Figure 2.5: (a) Space charge distribution in the depleted region at thermal equilibrium. (b) Schematic of E-field distribution. The area under the graph represents the built-in potential.

$$N_A x_p = N_D x_n. \tag{2.8}$$

From Fig.2.5(a) one can see that the depletion width may be written as:

$$W = x_p + x_n. \tag{2.9}$$

The gradient of the potential is equivalent to the E-field. By integrating

equations 2.6 and 2.7 one may calculate the E-field shown in Fig.2.5(b). The maximum field, E_m, occurs at x=0 and from the integrals:

$$E(x) = -\frac{d\psi}{dx} = -\frac{q}{\epsilon_s}(N_D)(x + x_p) \text{ for } -x_p \leq x < 0 \tag{2.10}$$

and

$$E(x) = -E_m + \frac{qN_D x}{\epsilon_s} = \frac{q}{\epsilon_s}(N_D)(x - x_n) \text{ for } 0 < x \leq x_n \tag{2.11}$$

setting x=0 gives:

$$E_m = \frac{qN_D x_n}{\epsilon} = \frac{qN_A x_p}{\epsilon_s} \tag{2.12}$$

Integrating again gives the potential, V_{bi}, the area under the graph in Fig.2.5(b):

$$\begin{aligned} V_{bi} &= -\int_{-x_p}^{x_n} E(x)dx \\ &= \frac{qN_A x_p^2}{2\epsilon_s} + \frac{qN_D x_n^2}{2\epsilon_s} \\ &= \frac{1}{2}E_m W \end{aligned} \tag{2.13}$$

The depletion width is defined as the active region of the detector. As such, it is important that its size be known accurately for particle detec-

tion. By combining Equations 2.8 to 2.12, one obtains an expression for the depletion width, W, as a function of V_{bi}:

$$W = \sqrt{\frac{2\epsilon_s}{q}\frac{N_A + N_D}{N_A N_D}V_{bi}} \tag{2.14}$$

One may manipulate the junctions by doping them with different concentrations. When the concentration of one region is much higher than the other, this is known as a "one-sided abrupt junction", Fig. 2.6(a). When the negative space charge region is more heavily doped than the positive, the distribution of the space charge is as shown in Fig. 2.6(b).

The depletion width of the p-side is much less than that of the n-side, $x_p << x_n$. Applying these conditions, equation 2.14 can be simplified to:

$$W \simeq x_n = \sqrt{\frac{2\epsilon_s}{qN_D}} \tag{2.15}$$

while the electric-field distribution is similar to equation 2.11 and decreases to zero at x=W so that:

$$E_m = \frac{qN_B W}{\epsilon_s} \tag{2.16}$$

where N_B is the lightly doped bulk concentration. Combining equations 2.11 and 2.16 gives the electric field, as shown in Fig. 2.6(c):

$$E(x) = \frac{qN_B}{\epsilon_s}(-W + x) = -E_m(1 - \frac{x}{W}) \tag{2.17}$$

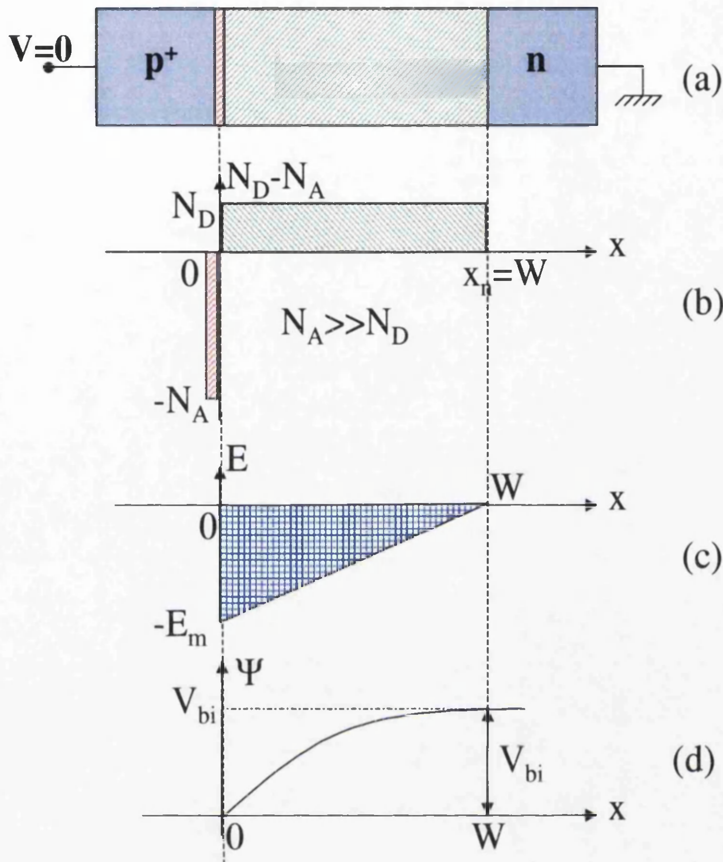

Figure 2.6: A schematic representation of (a) a one-sided abrupt junction with $N_A >> N_D$ (b) Space charge distribution (c) Electric-field distribution (d) Potential variation with distance, x.

Integrating Equation 2.17 and substituting Equation 2.14 gives an expression for the potential:

$$\psi(x) = \frac{V_{bi}x}{W}(2 - \frac{x}{W}) \tag{2.18}$$

The potential distribution is shown in Fig. 2.6(d).

2.3.2 Bias Voltage

Generally, a p-n junction is operated with an external bias voltage applied. This section will deal with the different operating modes of a diode and how these affect the depletion width. As has been shown, the potential across the unbiased junction is given by V_{bi} and the potential energy step from the p-side to the n-side is given by qV_{bi}. Figure 2.7 is a schematic representation of a junction under various bias conditions. By applying a positive voltage V_F across the junction, forward bias, current flows from the p-side to the n-side. The total potential across the junction decreases by V_F, as shown in Fig. 2.7(b), and as a result the depletion width decreases, reducing the sensitive area of the device.

If a voltage V_R is applied to the n-side so that current flows from the n-side to the p-side, the device is under reverse bias. The width of the depletion layer is increased as shown in Fig. 2.7(c). Substituting these conditions into Equation 2.15, an expression is obtained for the depletion width as a function of voltage:

$$W = \sqrt{\frac{2\epsilon_s(V_{bi} - V)}{qN_B}} \tag{2.19}$$

For forward bias, V is positive in Equation 2.19. From this relation it can be seen that the depletion width, W, varies with the square root of the voltage applied across the junction, V, when $V \gg V_{bi}$.

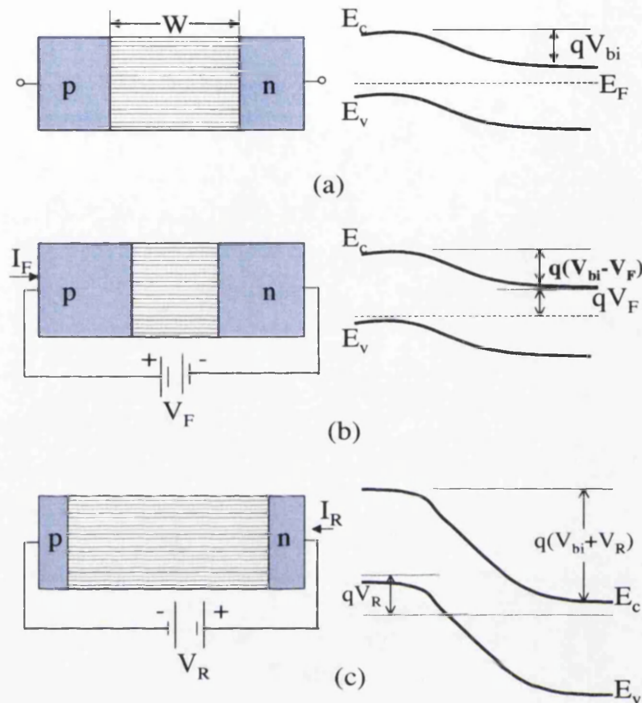

Figure 2.7: Schematic representation of depletion layer width and band bending of a p-n junction under (a) equilibrium conditions (b) forward bias and (c) reverse bias conditions.

2.3.3 Depletion Capacitance

Capacitance measurements over a junction are useful as they give an idea of the impurity concentration, N_B, present in the substrate. The capacitance per unit area is defined as:

$$C_j = \frac{dQ}{dV} \tag{2.20}$$

Combining this with dE=dQ/ϵ_s (from Poisson's equation) one may formulate an expression for capacitance with the approximation of dV to WdE. This yields:

$$C_j = \frac{\epsilon_s}{W} \text{ F/cm}^2 \tag{2.21}$$

This equation, for the depletion capacitance per unit area, is the same as the expression for a parallel plate capacitor, where the distance of separation of the two plates may be compared to the depletion width. This situation is only true for reverse bias where the space charge region has a very low concentration variation. For a forward bias device this is not true as a large current may flow through the junction. Combining Equation 2.21 with Equation 2.19 from Section 2.7, one obtains an expression for capacitance related to the applied voltage:

$$C_j = \sqrt{\frac{q\epsilon_s N_B}{2(V_{bi} - V)}} \tag{2.22}$$

Plotting $1/C^2$ versus V would produce a straight line for a one-sided abrupt junction. The gradient of the line allows the calculation of the impurity concentration, N_B, and the intercept on the V axis gives the built-in potential, V_{bi}.

2.4 Signal Generation

When an ionising particle passes through the detector, it imparts energy to the lattice and creates electron-hole pairs. At room temperature, 3.6eV are required on average to produce an electron hole pair [11]. The electron-hole pairs created via these interactions are detected as electric signals at the electrodes. After the interaction with an atomic electron, in the intermediate energy case, part of the energy will be absorbed by the semiconductor and converted into ionisation energy, while the remainder produces thermal energy. When the deposited energy is large enough then the signal will fluctuate around a mean number of charge carriers, N, given by:

$$N = \frac{E}{\epsilon} \tag{2.23}$$

where E is the absorbed energy and ϵ the mean energy spent for creating an e-h pair. The variance in the number of signal electrons (or holes) N is given by:

$$\langle \delta N^2 \rangle = F.N = F.\frac{E}{\epsilon} \tag{2.24}$$

where F is the Fano Factor. This gives the departure of the observed statistical fluctuations in the number of charge carriers from pure Poisson statistics. For silicon the theoretical Fano factor is 0.115 [12]. The electric field across the detector forces carriers to drift, according to their charge, to each electrode. The current received at the electrode is read out and

analysed. The route that a drifting carrier takes affects the charge signal that it produces on the electrodes so that understanding where the signal comes from is crucial. The accumulation of the charge signal is described by Ramo's theorem [13], and the various interaction processes that may occur and that are relevant for this work are discussed below.

2.4.1 Ramo's Theorem

In September 1939, Simon Ramo published a paper "Currents Induced by Electron Motion" [13]. This paper has been definitive, if at times misused, in describing charge carrier motion in semiconductor detectors. The carrier motion depends strongly upon the geometry of the device electrodes. For an accurate description of a device one must start with Poisson's equation [14][15][16][17]:

$$\nabla^2\psi = \rho/\epsilon \tag{2.25}$$

where ψ is the electric potential, ρ the charge density, and ϵ is the dielectric constant for the medium. This form must be used for an irradiated detector as it also considers the case of trapped charges. However, when there are no trapped charges, the Poisson equation reduces to the Laplace equation:

$$\nabla^2\psi = 0 \tag{2.26}$$

and one must choose an appropriate Laplacian operator for the geometry of the device under investigation.

Induced Charge

The charge carriers, namely electrons and holes, have different mobilities and drift velocities, thus their collection times are different. In silicon the electrons contribute to the fast component (ns) and the holes to the slower component (μs). This is compensated somewhat when interactions occur homogeneously through the detector, and the carriers have different distances to travel to reach the electrodes. The motion of the charge induces a current due to displacement of charge as it drifts towards the collection electrode. A useful concept in applications of Ramo's theorem is that of the weighting field and weighting potential [18][19], ψ_o. The weighting potential must be found from solving Equation 2.25 or Equation 2.26 for the correct detector geometry. The instantaneous current induced on an electrode is given by:

$$i = q\vec{v}.\vec{E_o} \tag{2.27}$$

where q is the charge of the carrier, $\vec{v}$ the drift velocity of the carrier, and $\vec{E_0}$ the aforementioned weighting field. By integrating Equation 2.27 it is possible to get the charge on the electrode, Q, due to charge carrier transport over a path within the weighting field, corresponding to a change in weighting potential $\Delta\psi_0$:

$$Q = q\Delta\psi_o \tag{2.28}$$

In essence, the moving carrier only contributes to the total charge if it moves through the electric field. One must impose certain assumptions. The voltage on the electrode on which the induced charge is to be calculated is set to unity. The voltage on all other electrodes is set to zero. If the Laplacian is used, one must ignore all trapped charge. It is important then to note that for radiation damaged detectors, one cannot assume a Laplacian approximation.

2.4.2 Charge loss

Radiation damage may cause loss of signal charge to the trapping by acceptor and donor levels with the energy bands. The signal charge will not be measured by the amplifier if the transit time lies outside the shaping time. The probability of signal charge collection is given by P=exp(-t/τ), where t is the collection time given by drift distance divided by drift velocity, v, and τ is the de-trapping time. The occupancy of a defect level is given by Fermi-Dirac statistics:

$$F(E) = \frac{1}{1 + exp(E - E_F)/kT} \tag{2.29}$$

So that the probability of occupation of a single defect level may be calculated. The probability of emission is given by:

$$\epsilon_s = v_{th}\sigma_n n_i exp(E_t - E_i)/kT \tag{2.30}$$

It can be seen then that deep levels will give a higher contribution to electron generation, which may be calculated from:

$$G_n = N_t F(E) \epsilon_n \tag{2.31}$$

2.4.3 Alpha Particles

Conventional characterisation of silicon detectors is most simply performed with alpha radiation. 5.5MeV alpha particles from an Americium-241 source travel only 28μm [20][21] into silicon. Most of the energy is released at this depth, creating electron-hole (e-h) pairs in the semiconductor bulk. According to Ramo's theorem, the drift of carriers will generate charge, collected at the output electrode. One may then be selective of the type of carrier to examine by choosing the front or backside, p-side or n-side[1], for irradiation. As long as a field is present in the bulk, signal will be collected due to the drift of carriers to the electrodes. This means that even with a device that is not fully depleted, (the electric-field not extending across the entire bulk (Fig. 2.6)), one will be able to collect a signal. However, this does not allow investigation of the entire bulk of the detector.

2.4.4 Minimum Ionising Particles (MIPS)

Minimum ionising particles traverse the bulk of the detector so collection of both electrons and holes from the entire bulk is possible. The specific

[1] This will be the convention adopted throughout this dissertation.

energy loss of a single charged particle travelling at velocity, v, in a medium of atomic number, Z, is given by the Bethe-Bloch formula [3]:

$$\frac{dE}{dx} = D_e(\frac{Z_1}{\beta_1})^2 n_e[ln\frac{2m_ec^2\beta^2\gamma^2}{I} - \beta^2 - \frac{\delta(\gamma)}{2}] \tag{2.32}$$

where $D_e=4\pi r_e 2m_ec^2$, and r_e is the classical electron radius. Z_1 the atomic number, n_e the number of electrons per unit volume, $\beta=$ v/c and γ the Lorentz factor, $(1-\beta)^{-1/2}$, I the mean ionisation potential, and δ a density correction factor. This is shown graphically in Figure 2.8.

A MIP generally releases energy homogeneously as it traverses the semiconductor, although there is a probability of high energy δ-rays. The charge signal is normally histogrammed using a multi-channel pulse-height analyser (MCA), allowing one to assign an appropriate energy range to the binning of the data. The peak count position will change with the signal collected to a higher position if more charge is collected, the latter normally coinciding with increasing reverse bias voltage (and hence increasing depletion region size) or decreasing temperature. The signal is proportional to d^2, where d is the depleted thickness, according to Ramo's theorem.

2.4.5 X-rays

^{241}Am is commonly used in detector characterisation as it emits both α and γ radiation, allowing one to probe the detector at different levels. The characteristic emissions from an ^{241}Am source are shown in Table 2.1:

From Table 2.1 it is evident that the 60keV γ's from ^{241}Americium give the largest signal. The source also emits characteristic L-series X-rays with

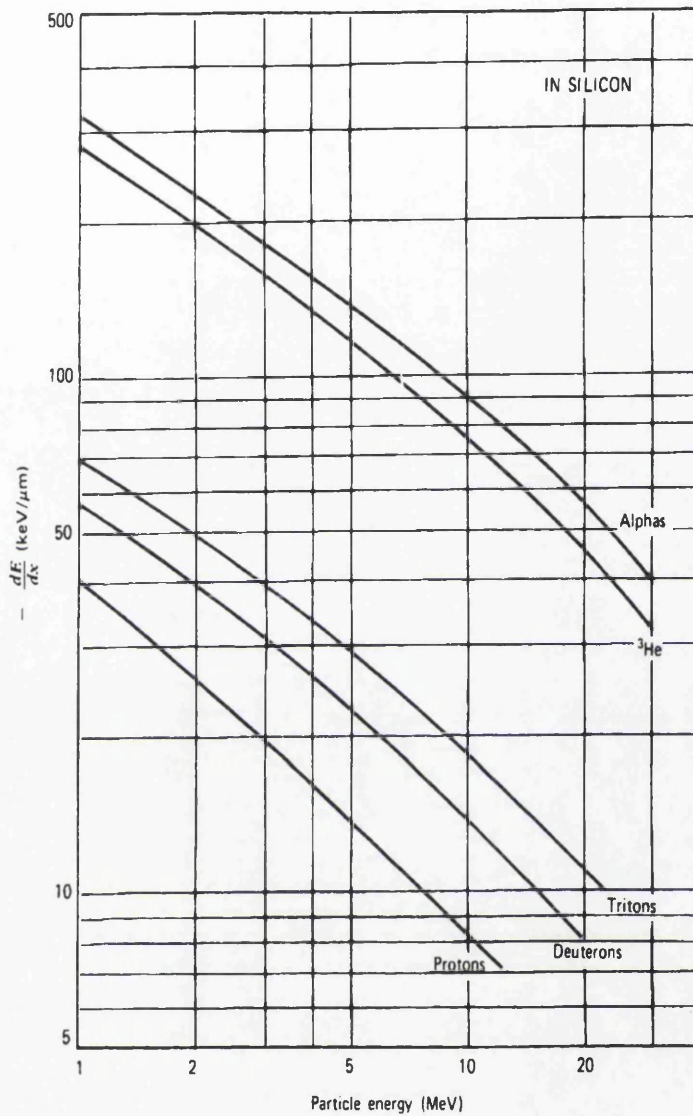

Figure 2.8: Energy loss rate in silicon for different high energy particles [22].

energies $\leq$ 20keV. Energy loss by X-ray photons is via three different mechanisms that dominate at different energies, namely the photoelectric effect, the Compton effect, and pair production.

From Graph 2.9 it can be seen that below a gamma ray energy of ~1MeV,

Photon Intensities per Disintegration of ^{241}Am		
Line	Energy(keV)	Percentage per Disintegration
L-α	13.9	13.3±0.4
L-$\eta\beta$	17.8	19.4±0.6
L-γ	20.8	4.9±0.2
γ	26.35	2.4±0.1
γ	59.54	35.82±0.12

Table 2.1: Photon Intensities per Disintegration of ^{241}Am

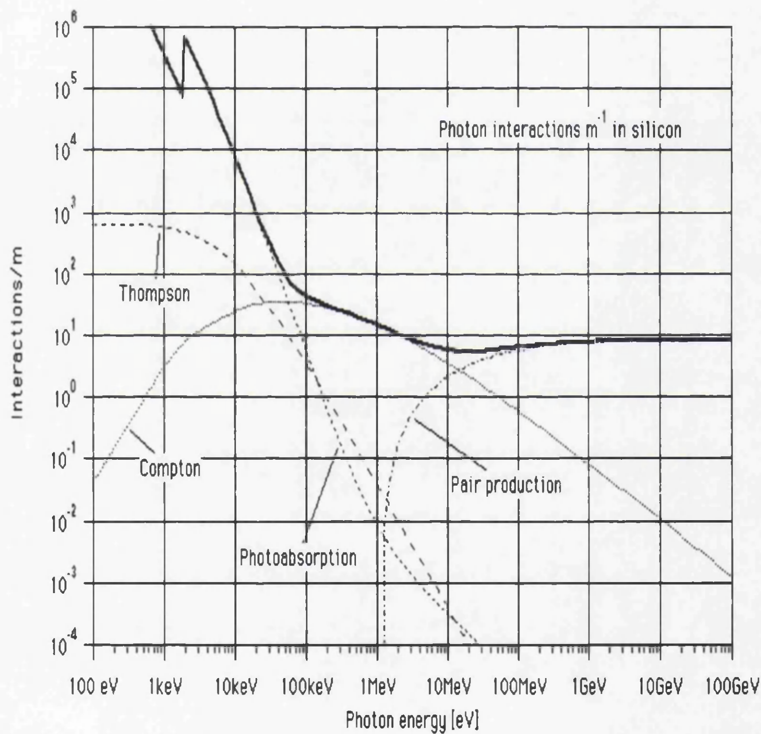

Figure 2.9: Graph of the variation of photon interaction cross-sections with photon energy. [23]

pair production does not play any role, and so is not an issue for the analysis described here. An X-ray photon deposits its energy much more locally than a MIP. This means that the 60keV photo peak position on the MCA should be constant for a fully depleted non-irradiated detector, (assuming no charge trapping) regardless of bias voltage. For a uniform probability of photon interactions across the detector thickness, the count rate, plotted on the ordinate-axis of the MCA display, is proportional to the active thickness of the detector and will depend upon the bias applied and the temperature of operation.

2.4.6 Photoelectric Effect

The photoelectric effect dominates at lower energies. An X-ray photon interacts with an inner, bound electron of the atom and is absorbed, and a bound electron is ejected, as illustrated in Fig 2.10.

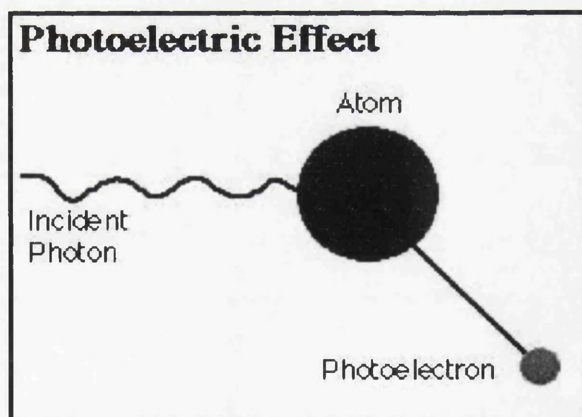

Figure 2.10: Schematic representation of the photoelectric effect.

In the energy region of ~60keV, the photoelectric cross-section varies with

photon energy, E, roughly as $E^{-7/2}$. For a 60keV photon the cross-section is $\sim$8barns/atom in silicon.

2.4.7 Compton Scattering

The Compton effect becomes significant at intermediate energies, over-taking the photoelectric effect around 80keV, but is already significant at 60keV as shown in Figure 2.9. The resultant state is an ejected electron and less energetic scattered photon (inelastic scatter), as shown schematically in Fig 2.11.

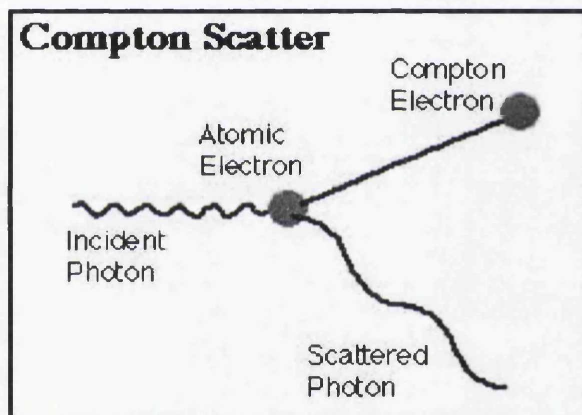

Figure 2.11: Schematic representation of the Compton effect.

2.5 Readout

As discussed, the electric field across the device forces each charge carrier to drift to the collection electrodes, holes to the cathode and electrons to the anode. Depending on where an interaction takes place inside the detec-

tor, the pulse rise time may vary, depending on which particles are collected first, while the total integrated charge will remain the same. It is important therefore to consider only a certain time interval after the interaction. Immediately after the interaction the carriers begin to drift and so will induce a displacement current. This gives an instantaneous signal which will continue until all charge carriers are collected. Beyond this time only noise charge, or leakage current, will be collected. The signal amplifier "shaping time" is of paramount importance for optimising the signal-to-noise ratio. While there are essentially two types of signal pre-amplifiers that may be used, charge or current sensitive, the work described in this thesis considers energy analysis and hence uses only a charge sensitive pre-amplifier.

2.5.1 The Charge Sensitive Amplifier

The charge sensitive amplifier, used in conjunction with semiconductor detectors [24], has a large input impedance, predominantly capacitive, and is used for energy analysis. The high impedance is obtained by having a low noise FET on-board the amplifier. The amplifier used for this work was the ORTEC 142A. It is optimised for low noise and fast timing, $\leq$5ns [25], and for a detector with a capacitance $\leq$100pF.

2.5.2 Pulse Shape

The preamplifier output pulse shape depends strongly upon the point of interaction, but will lie between the two extremes (a) and (b) of Figure 2.12.

As X-rays may interact at any point within the bulk, the generated charge carriers' drift distance may vary widely and so the shaping time must be

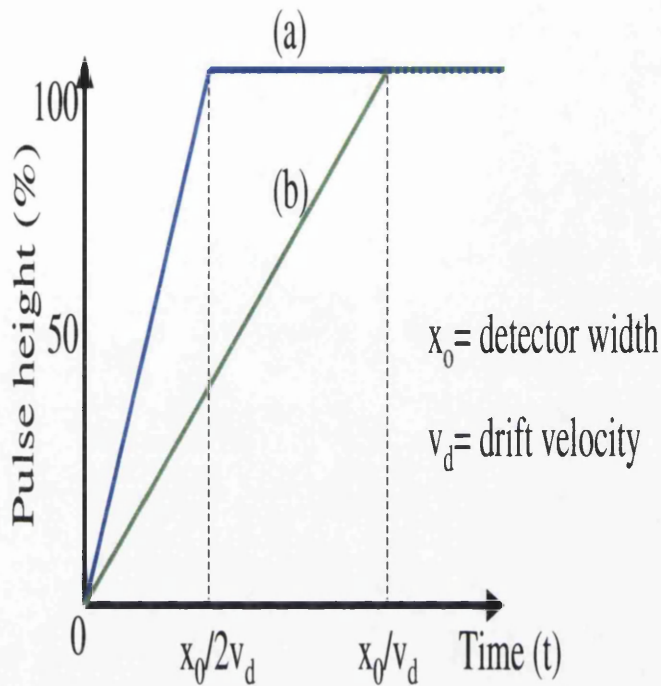

Figure 2.12: Expected charge pulse shapes in an ideal detector of planar geometry for (a) an interaction in the central region and (b) an interaction near one of the collection electrodes.

optimised. The "rise time" of the voltage pulse depends mainly on three things: 1) charge transit time, 2) the integration time constant from the amplifier input impedance, and 3) the amplifier's rise time. For a standard planar detector, the equivalent circuit may be drawn as in (Fig 2.13):

For a planar detector with active surface area, A, depletion width, W, and total thickness D, with material of resistivity ρ, one may construct the following relationships. The depletion zone capacitance, C_o, may be written as:

$$C_o = \frac{\epsilon_s A}{W} \tag{2.33}$$

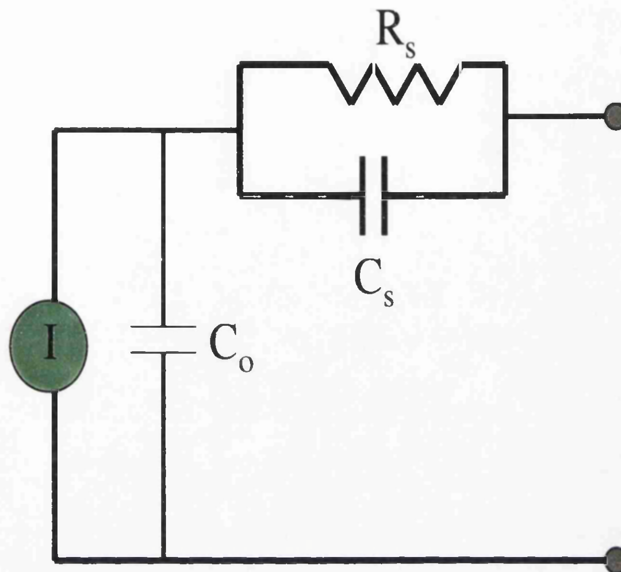

Figure 2.13: Simplest equivalent circuit of detector with planar geometry. The ohmic resistance of the reverse biased junction is not shown here due to its very high value.

The undepletioned zone resistance, R_s, may be calculated using:

$$R_s = \frac{\rho(D - W)}{A} \tag{2.34}$$

furthermore, the undepleted zone capacitance is given as:

$$C_s = \frac{\rho \epsilon_s}{R_s} \tag{2.35}$$

Knowing these values allows one to calculate the charge from the voltage pulse by:

$$V(t) = \frac{A_o}{C_o + C_t} Q(t) = \frac{A_o}{C_o + C_t} \int_0^t I(t) dt \qquad (2.36)$$

where A_o is the amplifier gain and $C_t = C_o + C_A$, where C_A is the amplifier input capacitance.

2.6 Summary

Having gained an appreciation of silicon detector material and how one may fabricate devices, extract signals, and interpret different types of interactions, one may now consider irradiation of devices. p-n junctions fabricated on float zone silicon are used for the work in this thesis. Charge collection by manipulation of depletion width is discussed in Chapter 4. X-rays are used to analyse devices here, although the interaction within the bulk of other types of radiation is important as it allows one to understand the mechanisms that occur within the detector.

Chapter 3

Detector Irradiation

3.1 Motivation

Semiconductor detectors are used over a wide range of fields, from medical imaging to particle physics. Common to all applications is exposure to radiation-induced damage. Without protection from continuous exposure to the radiation damage effects the detector performance would deteriorate and eventually the detector would fail completely. In order to increase the resistance to radiation, semiconductor detectors are tested with various forms of ionising radiation and their responses monitored, with the aim of revealing ways to make them more robust. Different types of radiation have different effects on the semiconductor material depending on the energy of the particle involved in the interaction and its charge. The characteristic damage to the periodic lattice induced by particular radiation must be identified. If an understanding of how it affects the signal can be obtained it may be possible to neutralise contributing defects. The methods used in this report include I-V measurements, Microwave Absorption, Deep Level Transient Spectroscopy

and the Transient Current Technique, the basic principles of all of which are introduced in this chapter.

3.2 Radiation Defects

As particles penetrate the detector, the release of energy may displace atoms from the silicon lattice, leaving lattice vacancies and interstitials (see Fig.3.1).

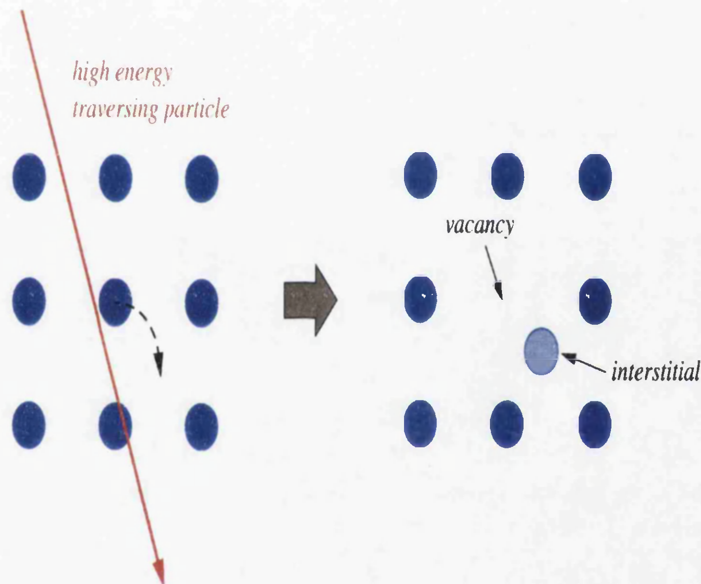

Figure 3.1: Schematic of irradiated silicon lattice.

These, and other defects resulting from the formation of defect complexes (clusters), have energy levels within the band gap and act as electron and hole traps. As an ionising particle passes through the silicon, for every 3.6eV energy it loses on average, an electron hole pair is produced. An electron may travel across the forbidden gap leaving behind a hole carrier. If the bandgap is devoid of defects the electron and hole may pass easily through the lattice

to the contacts to be interpreted as signal charge. If the silicon has been irradiated and has hence suffered radiation-induced damage in the form of lattice defects, the band structure will be altered. Radiation-induced defects have associated energy levels which lie within the bandgap and each defect has a distinctive energy, and individual, temperature dependent electron or hole capture and emission cross-sections. For a defect level below the conduction band but above the Fermi level the probability of (vacancy related) electron capture is high, whereas for a defect level above the valence band but below the Fermi level,(interstitial related) hole capture is more probable (Fig.3.2).

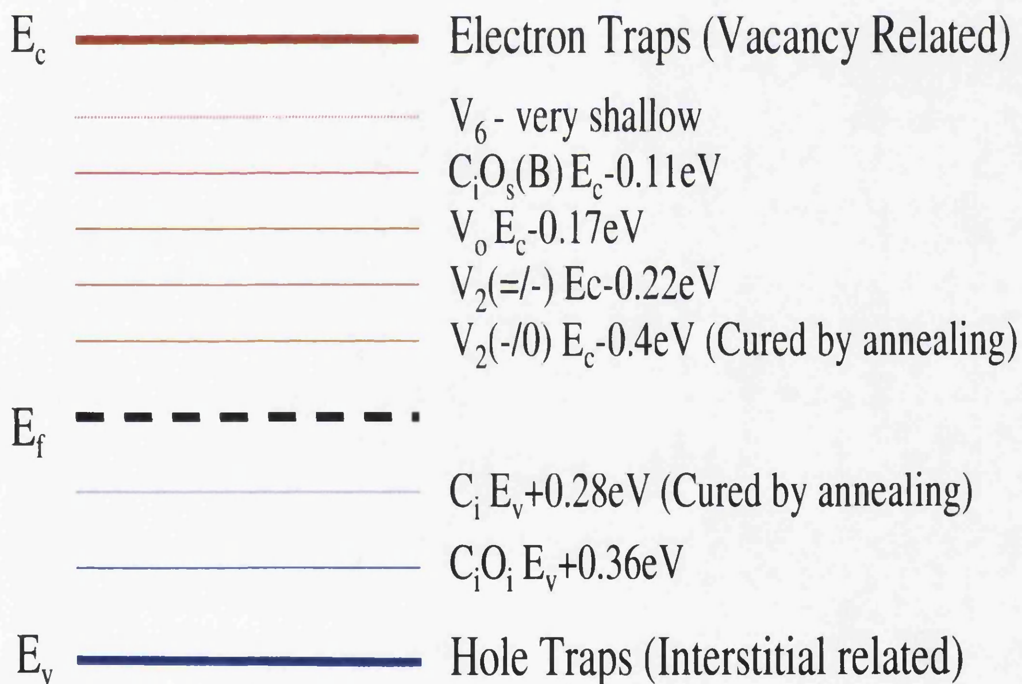

Figure 3.2: Schematic of some of the radiation-induced trap levels in the silicon energy band.[26]

Defects are free to move in the crystal lattice and can form complexes with each other. Although a wide spectrum of defect energy levels has been identified across the bandgap in silicon [10] this work concentrates specifically on the di-vacancy V_2, and the complexes with oxygen, V_O, and carbon, forming C_i-O_i. The former has an energy which lies 0.17eV below the conduction band and can be annealed out while the latter lies 0.36eV above the valence band. These complexes have different cross-sections and hence a different capacity to absorb carriers. They also have a charge which will determine which type of carrier they may absorb. The cross-section and charge of a trap will change depending on what type of carrier is trapped. Knowing what defects are present after irradiation and how these affect the detector performance is of paramount importance. By analysis it may be possible to determine how to neutralise degrading effects that defects have on the semiconductor detectors and enhance the beneficial effects.

3.3 Preventions and Cures

As different types and energies of radiation affect a semiconductor in different ways, extensive investigations have been performed by many groups, in particular by the ROSE Collaboration (RD48, CERN) [27]. The Non-Ionising Energy Loss (NIEL) hypothesis [28], introduced below allows one to normalise the effects of given fluences of different types of radiation to an equivalent fluence of 1MeV neutrons by scaling by a "hardness" factor given in Figure 3.3 [10]. One can imagine a situation where the optimisation of a detector for a particular radiation environment is possible. Adding impurity oxygen to the silicon has been shown to prolong the detector's lifetime

against proton and pion bombardment [10]. The oxygen, however, appears to have no significant effect against 1MeV neutron irradiation. At a macroscopic level one can also improve the performance of silicon detectors by altering the temperature of operation. An example of this is the "Lazarus Effect", studied by the RD39 Collaboration, CERN [29]. Investigation of this effect makes up a large portion of the work described in this thesis and is introduced here, with the author's experimental results and conclusions shown later.

3.3.1 NIEL Scaling Hypothesis

Silicon semiconductor detectors used in high radiation environments encounter hadronic and leptonic particles. Charged hadrons interact via the Coulomb mechanism at lower energies and cause ionisation of lattice atoms in a process which is reversible in silicon. Neutrons interact with the nucleus and react via elastic scattering and nuclear interactions above 1.8MeV. These two types of radiation affect the silicon in different ways at different energies and fluences, but they may be compared by the NIEL hypothesis. The NIEL hypothesis assumes that any displacement damage induced in the material by irradiation may be scaled linearly with the amount of non-ionising energy imparted in the collision. Neither the spatial distribution nor the annealing of the defects contradicts the hypothesis.

Each interaction releases a Primary Knock-on Atom (PKA) with recoil energy, E_R. The proportion of the recoil energy that contributes towards the displacement damage may be calculated using the Lindhard partition function, $P(E_R)$[28]. Using this function the NIEL can be calculated and

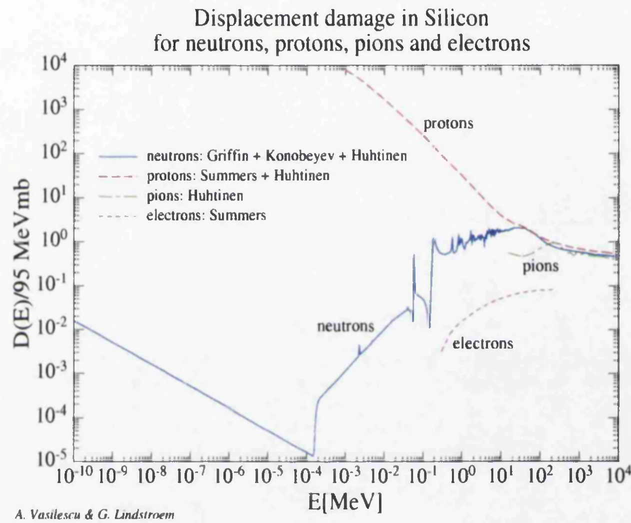

Figure 3.3: Displacement damage function, D(E), in silicon showing the "hardness factor" values one may use to normalise radiation dose for pions, protons and electrons to that for 1MeV neutrons [30][31][32][33][34].

expressed as the displacement damage cross-section, D(E), given by:

$$D(E) = \sum_{\nu} \sigma_{\nu}(E) \int_{0}^{E} f_{\nu}(E, E_R) P(E_R) dE_R \qquad (3.1)$$

This equation represents the damage done by all possible interactions, ν, with cross-section σ_{ν}, between an incoming particle with energy, E, and the silicon lattice. f_{ν} represents the probability of generating a PKA with recoil energy E_R. The electric field inside a detector, operated under reverse bias, extends from a maximum at the p^+ contact, and as the bias voltage increases, the field extends through the n-type bulk, with a minimum at the n^+ contact. The full depletion voltage is proportional to the square of the detector thickness and may be written as:

$$V_{dep} = \frac{q_0}{2\epsilon\epsilon_0} N_{eff} d^2 \qquad (3.2)$$

This remains true even after the space charge region sign inversion, the removal of donors, and an increase in the concentration of acceptor defects. In addition to "beneficial annealing", (short term annealing of some of the radiation damage over a time scale of the order of days), the radiation damaged silicon also exhibits long term (over a timescale of months to years) so-called "reverse annealing", which is in fact detrimental to the detector performance. The latter is strongly linked with defect kinetics and hence with temperature, permitting the control of the time scale of the reverse annealing by cooling. The timescale of reverse annealing may be increased and

its effects deemed negligible if the device is cooled to -10°C. Employing the 1MeV neutron equivalent fluence, ψ_{eq}, and the current related damage factor α, the leakage current is related to the temperature by [10]:

$$I(T) \propto T^2 exp(\frac{-2k_B T}{E_g}) \tag{3.3}$$

Leakage current is discussed in more detail in Section 3.4.1. contribution due to radiation damage may be calculated by:

$$I = \alpha\psi_{eq}V \tag{3.4}$$

where I is the measured leakage current at full depletion, V the volume, ψ_{eq} the 1MeV neutron equivalent fluence, and α is a current related damage factor that allows scaling. For n-type silicon at 20°C, α=8.0x10^{-17}Acm^{-1} [35], below type inversion fluence. This depends heavily on detector geometry, and hence it is important that a guard ring structure is used to define clearly the detector volume. The real power of the NIEL hypothesis is the ability to compare different types of irradiation, but furthermore, by measuring the increase in leakage current caused by the irradiation of the device the radiation dose may be calculated directly.

3.3.2 Oxygen Enriched Silicon

The RD48 Collaboration, of which the University of Glasgow is a member, is striving towards the development of more radiation-hard silicon using various techniques of defect engineering through ion implantation. From an

in-depth investigation of defect production through irradiation, the Collaboration postulated that a "getter" agent in the material could be used to collect the defects and improve detector performance. Of the various agents tried, oxygen proved to be the most successful. One may compare the damage by using the rate at which defects are introduced into the material. A *pnn* diode detector will undergo a transformation to a *ppn* diode beyond a certain dose. The space charge sign inversion results from the donor concentration being compensated by radiation-induced acceptors, with the result that N_{eff} goes through a minimum, where the conduction of the material switches polarity from n-type to p-type. Continuing to irradiate beyond this point introduces further deep acceptors at a rate β, which may be extracted from the slope of a graph of N_{eff} vs 1MeV neutron equivalent fluence. Figure 3.4 shows such a graph for oxygen enriched diodes irradiated with neutrons, pions, and protons.

The oxygen enriched diodes perform well when irradiated with protons and pions, charged particles. However, the β value for neutron irradiation is unchanged. The difference in response to charged particles and to neutrons is not yet understood.

3.3.3 The Lazarus Effect

Silicon semiconductor detectors are generally operated at room temperature or cooled to around -10°C. This reduces the leakage current and hence the noise. Another consequence of the reduced temperature is the reduced thermal energy in the lattice. At room temperature the electrons and holes have sufficient energy to trap and de-trap over a timescale of seconds and minutes.

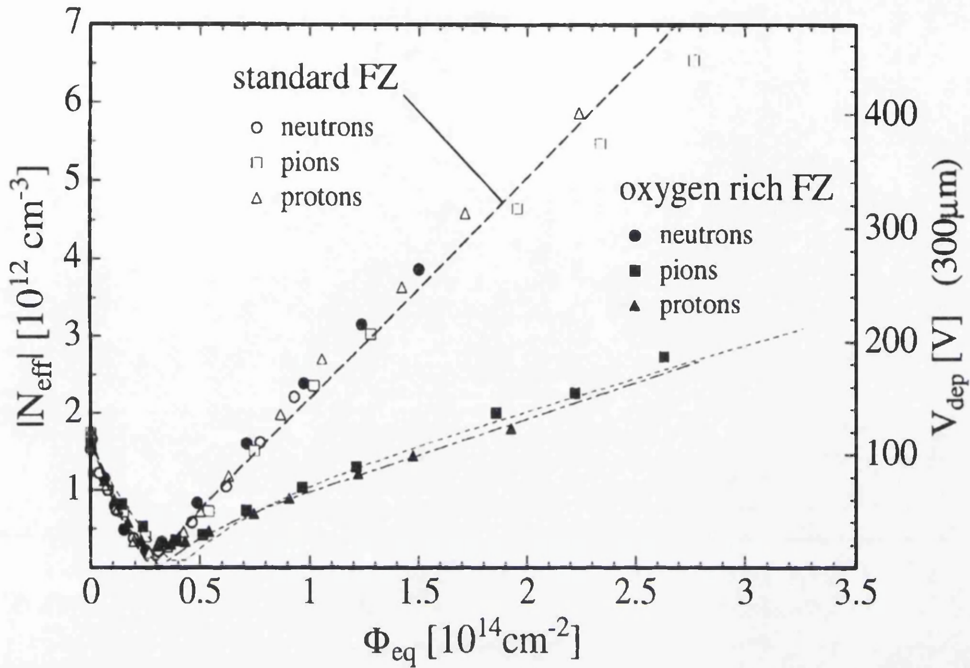

Figure 3.4: Comparison of standard float zone silicon and oxygen enriched silicon when irradiated with protons, pions, and neutrons [10].

The trapping time, τ_t, and de-trapping time, τ_d, are temperature dependent as described by [36][37]:

$$\tau_t = \frac{1}{\sigma_\nu V_t(T) N_t} \tag{3.5}$$

and

$$\tau_d = \frac{1}{\sigma_\nu V_t N_c exp\left(\frac{-E_t}{kT}\right)} \tag{3.6}$$

where the subscript ν denotes either electrons or holes and σ_ν is the cross-section, N_t is the concentration of deep levels and equals the total number of deep traps minus the number of filled traps, $N_{c,v}$ is the density of states in the conduction or valence band, E_t the trap energy level in the band, V_t the thermal velocity, k the Boltzmann constant and T the temperature. The de-trapping time depends exponentially on temperature. As the temperature is decreased, the time for the trap to empty increases. By lowering the temperature to liquid nitrogen temperature, a trap may remain full on a timescale of many days and so becomes essentially frozen. Taking as an example the main traps studied here, as described in Section 3.2, it is instructive to notice the variation across the band gap, Table 3.3.3:

Comparison of Trapping and De-Trapping Times of Defects					
Defect	E_t(eV)	τ_{tn}[s]	τ_{dn}[s]	τ_{tp}[s]	τ_{dp}[s]
$VV^{-/0}$	E_c-0.42	3.4x10^{-7}	6.3x10^{5}	5.3x10^{-7}	2.7x10^{5}
C_iO_i	E_v+0.36	1.85x10^{-4}	7.26x10^{6}	2.41x10^{-7}	2.6x10^{13}

Table 3.1: Comparisons of trapping (subscript n denotes electron values) and de-trapping (subscript p denotes hole values) times of relevant defects as a function of the position in the bandgap.[38][39][40].

The values shown in Table are calculated for a detector irradiated to a fluence of Φ_n=1.4x10^{14}cm^{-2} and operated at 130K. A large fraction of the traps will become filled and, as the de-trapping time is comparatively long, the trap is essentially inactive. If all the traps are full and an incident ionising particle produces free carriers in the detector, they will no longer be trapped by the radiation-induced defects, but will contribute fully to the

collected signal. The efficiency of a detector is defined in terms of how well it collects charge, its Charge Collection Efficiency (CCE). For this work, an unirradiated silicon device is used as a reference detector. One assumes that such a detector is 100% efficient when fully depleted so that when a pulse height spectrum is taken of a fully absorbed ionising particle, the peak position corresponds to the energy of the incident particle.
The CCE of the device for minimum ionising particles is:

$$CCE \propto \left(\frac{W}{d}\right)^2 exp\left(\frac{-t_{drift}}{\tau_{trap}}\right) \tag{3.7}$$

where W is the *active thickness*, d is the total thickness of a detector, and the exponential term holds the time dependence: τ_{trap} is the mean trapping time for electrons or holes and t_{drift} is the carrier drift time through the detector. The *active thickness* of the detector, referred to as the Depletion Width, W, depends on the bias voltage, V, applied to the detector and on the *space charge density,* N_{eff}, and is given by [41]:

$$W = \sqrt{\frac{2\varepsilon\varepsilon_o V}{q|N_{eff}|}} \tag{3.8}$$

where ε_o is the relative permittivity of free space and ε is the relative permittivity of the material. From the de-trapping time Equation, 3.6,

$$\frac{1}{\tau_{trap}} \propto exp\left(\frac{-E_{trap}}{kT}\right) \tag{3.9}$$

where E_{trap} is the energy level of the trap, k the Boltzmann constant and T the temperature. From measurements made on irradiated devices [43], the optimum operating temperature for maximum CCE at minimum bias voltage is 130K (Fig. 3.5).

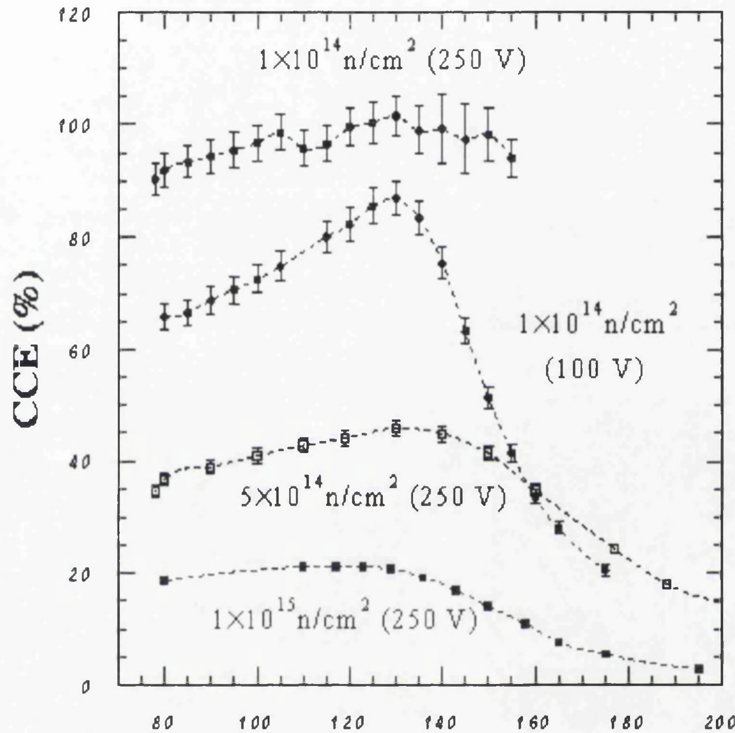

Figure 3.5: Graph showing various measurements made in irradiated devices [43]. The maximum CCE occurs at around 130K in all bias voltage cases, irrespective of the dose.

3.3.4 Experimental Set-up

The Lazarus Effect gives the optimum temperature at which the least bias voltage is required to deplete fully a silicon semiconductor detector. The following sections in Chapter 3 presents details of measurements that were

made using 400μm silicon detectors irradiated with 450GeV Pb ions at the CERN-SPS facility. The lead beam was delivered to the experimental hall and beam diagnostic measurements allowed a calculation of fluence. The beam size was a Gaussian form of 1mm allowing each pad to be irradiated separately to a different fluence. A summary is shown in Table 3.2.

The devices that were investigated are DC-coupled Al/p$^+$/n/n$^+$/Al implanted silicon detectors fabricated at Brookhaven National Laboratory (BNL), New York. The silicon is phosphorus doped and the backside, n$^+$, is uniformly implanted. The crystal is started on FZ n-type material oriented in the <111> plane[1]. The wafers are 100mm diameter and are 400μm thick. The passivation layer is 4700Angstroms thick SiO_2 after 6 hours at 1100°C in O_2 and TCA[2] bath. The aluminium layer is 2500Angstroms thick on both sides and forms a mesh to allow laser penetration after fabrication. The detector was in a 3x3 array format consisting of 9 individual silicon diode detectors with active areas of 1.5x1.5mm^2. For the investigation with the techniques described here, it was necessary to cleave the devices into single pad diodes. The devices were irradiated at CERN in a specially constructed cryostat operating on the same principle as described in [44]. A picture of the cryostat after installation is shown in Figure 3.6.

The cryostat is operated with a continuous flow liquid nitrogen supply to maintain a controlled temperature. The beam entered the cryostat through a thin stainless steal window. Scintillation counters mounted along the beam axis and an internal detector provided an event trigger. Measurements were made on the detectors *in situ*. By lowering the beam intensity by inserting a

[1]The BNL group have most experience with crystals grown in this way.

[2]a carbon containing material.

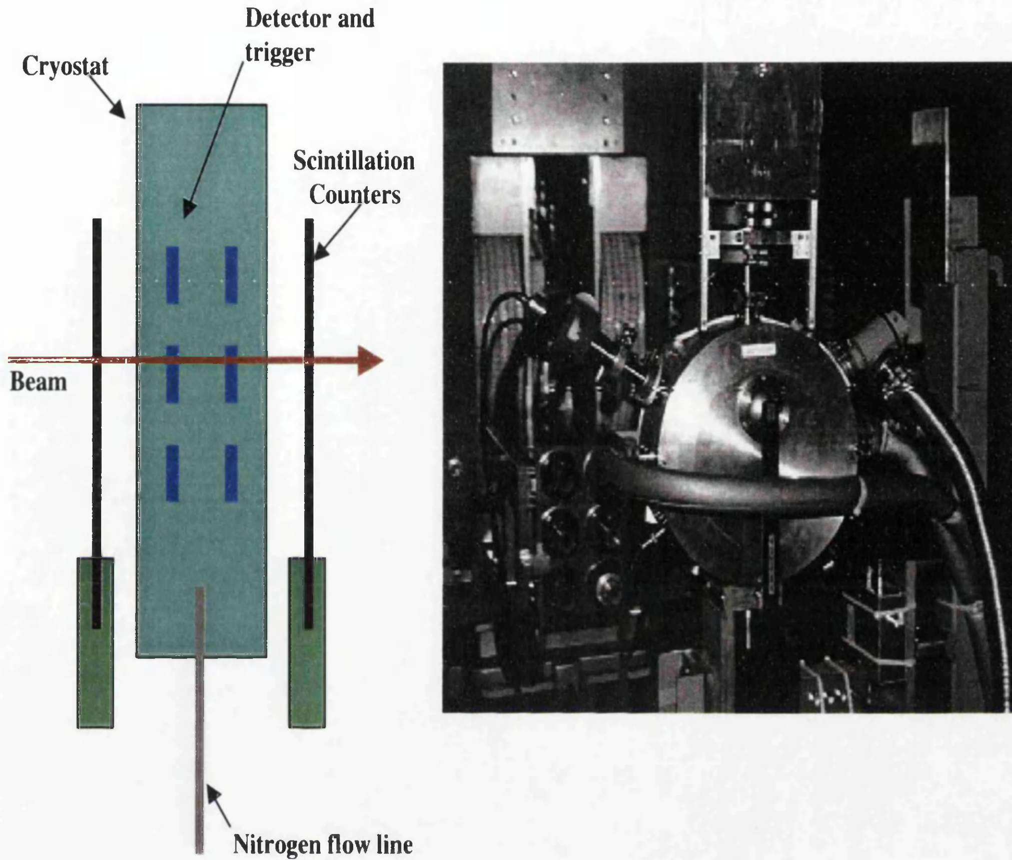

Figure 3.6: The image on the right is the cryostat used in the CERN SPS test beam area to irradiate silicon diodes held at near liquid nitrogen temperature. The left schematic shows the set-up inside the cryostat and also the trigger scintillation counters.

5cm Aluminium target 150m upstream from the experimental hall, reducing its energy to 300GeV, at pre-determined irradiation doses, it was possible to perform the voltage and temperature scans which are discussed in depth in Chapter 5. The scintillation counters were used for particle counting and triggering. LabVIEW was used for data acquisition and on-line analysis as

well as to control various detector parameters.

3.4 Detecting Defects

The presence of defects induced by radiation in a detector may be inferred from the increased leakage current and loss of signal amplitude. However, one must employ special techniques to investigate the damage to the lattice at the microscopic level. Combining the macroscopic with the microscopic data, one may build a picture of what is happening inside the detector.

3.4.1 I-V Measurements - Leakage Current

The leakage current in a diode that is operated in reverse bias mode is not only due to impurities in production but also to the defects that irradiation introduces. As the dose of irradiation increases, so does the leakage current. The leakage current has two components: bulk generation current, I_{bulk}, and surface generation current, I_s. The bulk generation current is due mainly to defects that exist close to midgap that contribute to electron-hole capture and re-emission. The surface current is due mainly to surface states, again caused by defects. These may be introduced by dangling bonds at the end of the periodic lattice, but are mostly due to the SiO_2–Si interface states. While surface damage is not an issue with neutron irradiation, it is with proton and pion irradiation, although the surface current produced is still much smaller than the bulk current. Only defects in the space charge region, deep donors or acceptors, contribute to the bulk current. As the bulk current is induced in the active region, it is also related to the active thickness, and hence the

applied voltage by:

$$I_{bulk} \propto W \propto \sqrt{V} \text{ , for } V \leq V_{dep} \tag{3.10}$$

Equation 3.10 saturates when the voltage reaches the depletion voltage. An associated generation lifetime, τ_g, may be defined from:

$$I_{bulk} \propto \frac{W}{\tau_g} \tag{3.11}$$

The strong temperature dependence of the leakage current is a bonus to operation at cryogenic temperature. This dependence may be written in terms of the leakage current I(T_{ref}) at a reference temperature T_{ref} as [39]:

$$I(T_{ref}) = I(T)(\frac{T_{ref}}{T})^2 exp(-\frac{E_g}{2k_b}\frac{1}{(}T_{ref} - \frac{1}{T})) \tag{3.12}$$

Performing I-V measurements on a diode allows one to compare with the perfect diode situation. From the leakage current one may calculate the dose of radiation that a detector has received.

3.4.2 Deep Level Transient Spectroscopy (DLTS)

This spectroscopic technique is used to characterise deep level defects in semiconductor materials, providing an individual spectral line response for each deep level detected. A trap's cross-section, concentration, and thermal activation energy may be determined by performing temperature scans. DLTS

uses capacitance, voltage or current transient signals resulting from pulsed changes in bias voltage applied to the device.

The junction will be held initially at reverse bias, as shown in Figure 3.7, at this point the states in the space charge region remain free of electrons. The voltage is then pulsed more positively with the consequence of reducing the size of the depleted region, (space charge), allowing majority carriers to be available for capture in the previously depleted region. For this example, the defects will be below the Fermi level and hence occupied with electrons. The trapped charge has the effect of altering the capacitance of the space charge region. When the pulse is removed, and negative bias voltage reinstated, the trapped charge is re-emitted into the conduction band, if thermal excitation is sufficient, and swept away by the potential across the device. Emission from traps reduces charge compensation and also space charge region width while increasing the capacitance. The time constant for this transient is given by the reciprocal of the emission rate of the defect, e_n. The characteristic time constants and amplitudes of capacitive transients are used to evaluate defect parameters.

The response time of the trapped electrons is relatively slow and heavily temperature dependent. As the electrons are emitted into the conduction band, a net positive charge remains, increasing space charge density. The difference between the two states of the system is measured many times and averaged. One may perform these measurements over a range of temperatures, analysing how the trap behaves and how its emission time varies with temperature. Measurements were made on a non-irradiated sample as described in Section 3.3.4. Figure 3.8 shows the DLT spectra measured.

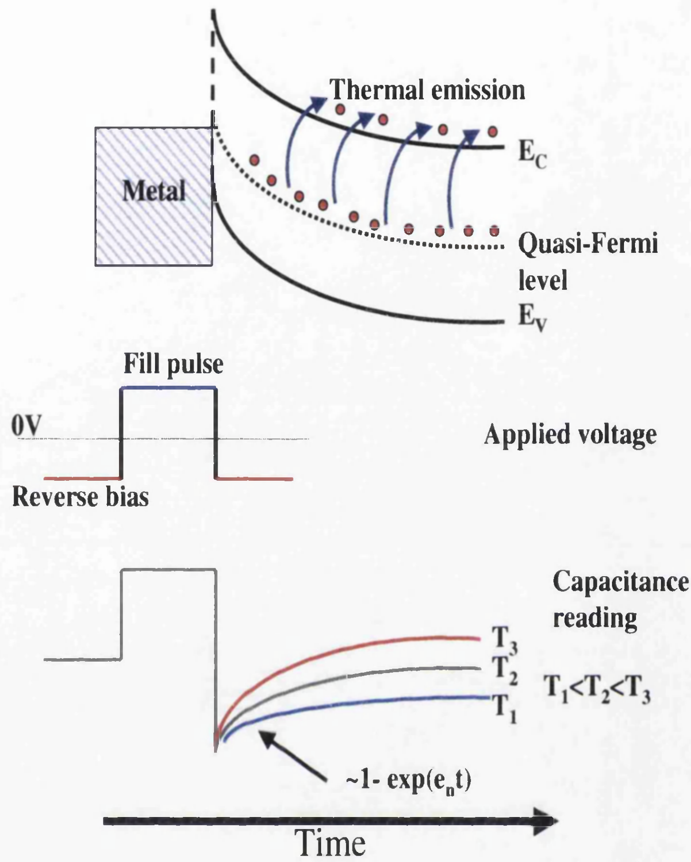

Figure 3.7: DLTS process showing initial forward bias pulse, then returning to negative bias and the corresponding capacitance transient [45].

The peaks correspond to the deep levels E_1=E_c-0.37eV and E_2=E_c-0.38eV with capture cross-sections of σ_1=3x10^{-14}cm^2 and σ_2=3x10^{-12}cm^2 respectively, determined from Arrhenius plots. Using a software based evaluation library, one may discern that these levels correspond to the impurities Pt and Ti, at low concentrations, $N_m/N_p<10^{-5}$.

Silicon samples were irradiated with 450GeV Pb-ions at the CERN SPS

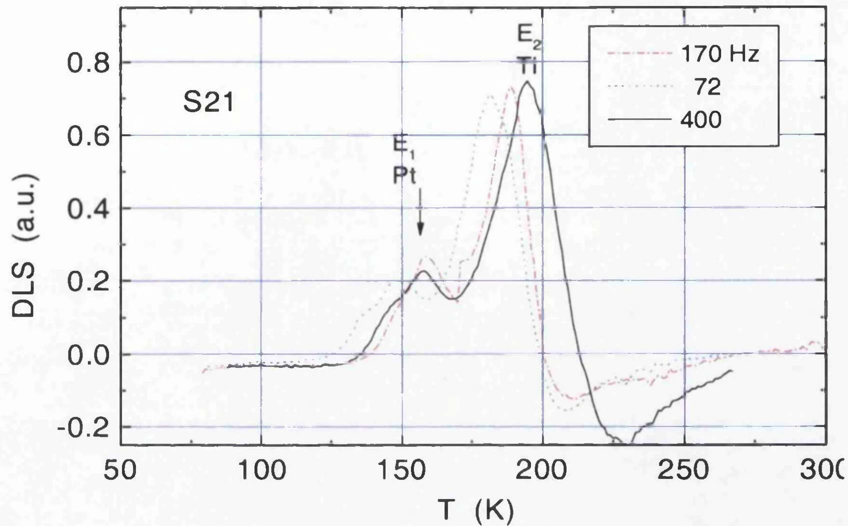

Figure 3.8: DLT spectra measured on a non-irradiated diode at different injection pulse duration and corresponding "lock-in" frequencies.

facility to the fluences shown in Table 3.2. Figure 3.9 shows DLTS signals for the moderately irradiated S07 and the non-irradiated device S21 is plotted in the same spectrum for comparison.

The irradiated device shows very different DLTS results than its non-irradiated counterpart. By varying temperature, excitation pulse duration, and lock-in frequencies, one may identify several peaks. From Arrhenius plots and evaluation software routines, one may identify the majority carrier traps with activation energies $E_1=E_c$-0.16eV, $E_2=E_c$-0.195eV, $E_3=E_c$-0.24eV, and $E_4=E_c$-0.46eV with corresponding capture cross-sections $\sigma_1=5\text{x}10^{-16}\text{cm}^2$, $\sigma_2=1.1\text{x}10^{-15}\text{cm}^2$,$\sigma_3=1.2\text{x}10^{-15}\text{cm}^2$, and $\sigma_4=5.6\text{x}10^{-16}\text{cm}^2$. Comparing the results with the evaluation software package and previous publication [47] results, one may ascribe the defects as follows: E_1 is an A centre (VO), E_2

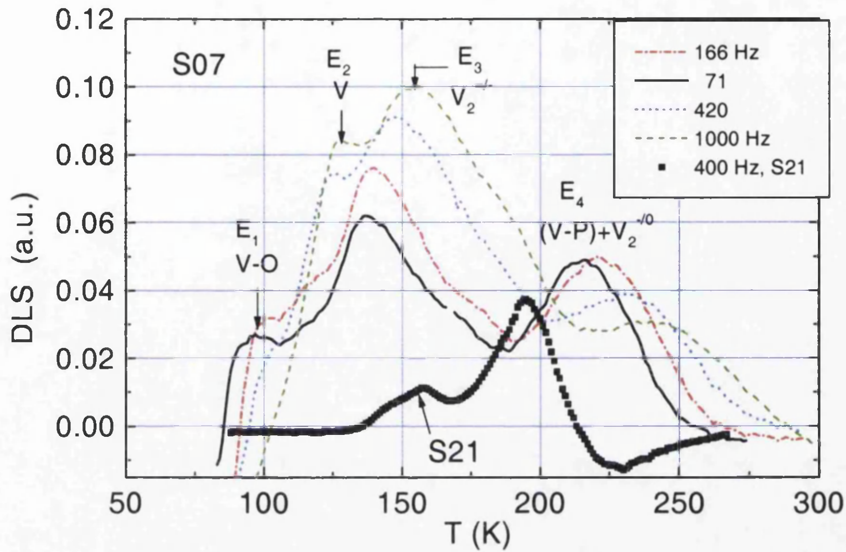

Figure 3.9: DLT spectra measured on the Pb-ion irradiated sample S7 and compared with unirradiated sample S21.

is caused by singly charged vacancies (V^-), E_3 is related to the di-vacancy ($V_2{}^{=/-}$) and E_4 is due to the E centre (PV) and di-vacancy ($V_2{}^{0/-}$). The DLTS seems to indicate that Pb-ion irradiation induces point like defects with vacancy associated centres, with the $V_2{}^{=/-}$ level dominant. For this type of irradiation point defect complexes and clustering appear to be the dominant defect types.

Figure 3.10 allows a comparison with proton, pion and neutron irradiation. The defects VO_i, C_iC_s and C_iO_i are attributed to point defects in the crystal lattice as expected from the unperturbed shape of the DLTS-signal [46].

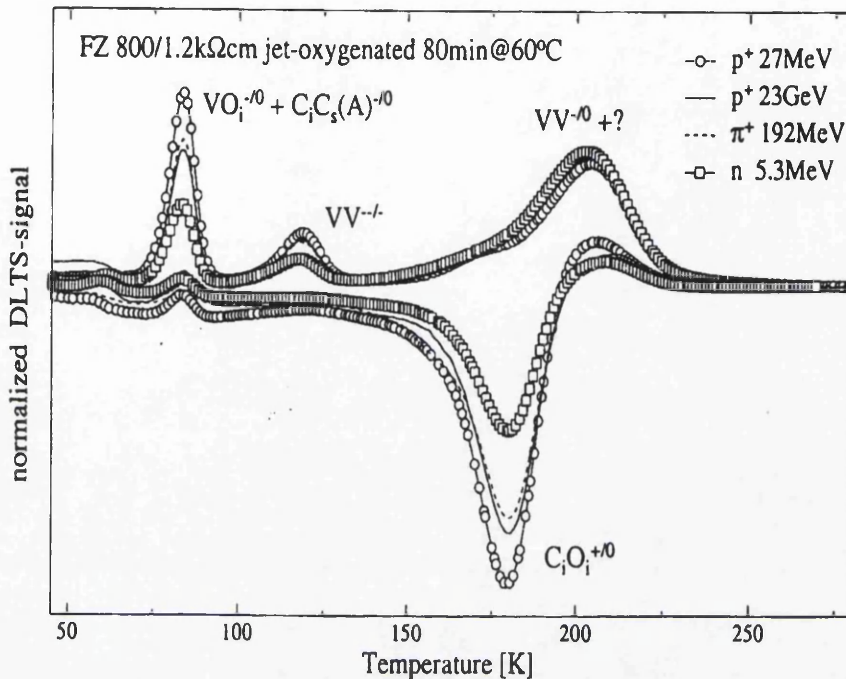

Figure 3.10: DLTS comparison [46]. for different irradiation sources.

3.4.3 Transient Current Technique (TCT)

The Transient Current Technique is an extremely powerful tool for analysing a single type of carrier in a detector. Applying a short red laser light pulse with wavelength $\lambda = 660$nm to one side of a device, penetrating $\sim 5\mu$m into silicon, one effectively injects non-equilibrium charge carriers. By illuminating the p-side, an excess of carriers will be produced very close to the p^+-contact. The electrons have only a short distance to travel before collection. However, the holes have much further to travel across the device. One may then use this technique to consider one type of carrier at a time. The transient signal is recorded using PC based data acquisition software

that allows averaging over the sample. For this to be successful one needs electronics with a fast rise and fall time, of the order of < 2ns. The laser pulses need to be shorter than 5ns so that one may assume a δ-pulse approximation for carrier generation in the detector material. One may distinguish between laser illumination of the back (hole drifting), and the front (electron drifting) so that the transient signal observed is either the hole current or electron current, respectively. The current pulse slope should in fact give an indication of the electric field strength across the device [51]. The pulse width for the electrons should be 2 to 3 times smaller than that for holes due to the difference in electron and hole mobility. TCT measurements were made on devices described in Section 3.3.4. The detectors were irradiated with varying doses and the results from TCT measurements shown in Figures 3.11, 3.12, 3.13, 3.14, 3.15, and Figure 3.16. These give an indication of excess carrier behaviour. SA was illuminated from p-side, electron drift. A second peak appears as bias voltage is increased but eventually a single peak evolves as the two depletion regions merge. SB is more heavily irradiated and illumination was from n-side, hole drift. Hole transient peaks are wider due to their lower mobility than electrons. SC is illuminated from the p-side. The sample has been irradiated to $1\text{x}10^{14}\text{cm}^2$ 1MeV neutron equivalent fluence. SD was also illuminated from the p-side and has been irradiated just beyond type inversion. SE was illuminated from p-side and has been irradiated to $5\text{x}10^{14}\text{cm}^2$ 1MeV neutron equivalent fluence. The laser injection current has also been increased from that of the previous measurements. SF is the same sample as SE but the laser injection current has been increased again, as has the bias voltage. The result is that the second peak is not clearly observed.

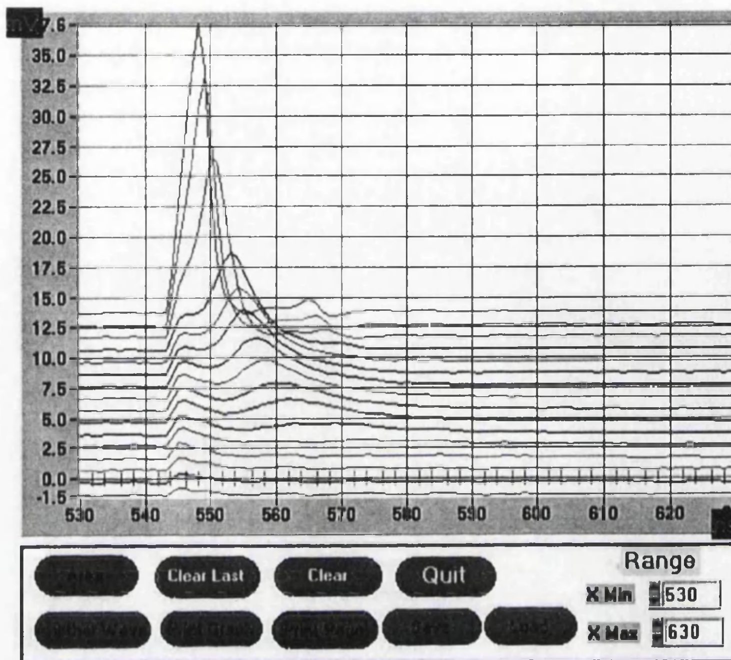

Figure 3.11: Sample A (SA) illuminated from p-side, electron drift

3.4.4 Microwave Absorption (MWA)

The microwave transient absorption technique is used to determine excess carrier lifetimes in a semiconductor detector. Figure 3.17 is a schematic representation of the experimental set-up for measurements on silicon diodes.

The Microwave absorption technique allows an investigation into device characteristics and structural imperfections of both the surface and bulk [48]. Measurements were carried-out by placing parallel excitation-probes over the sample. The laser light pulses were of the order of 10ns and the wavelengths used for excitation were 532nm and 1064nm. By using dual excitation wavelength modes a simple nomograph technique [49][50] allows the separation of surface recombination rate and bulk carrier lifetimes. The short pulse duration permits δ-pulse approximation of the excess carrier generation in

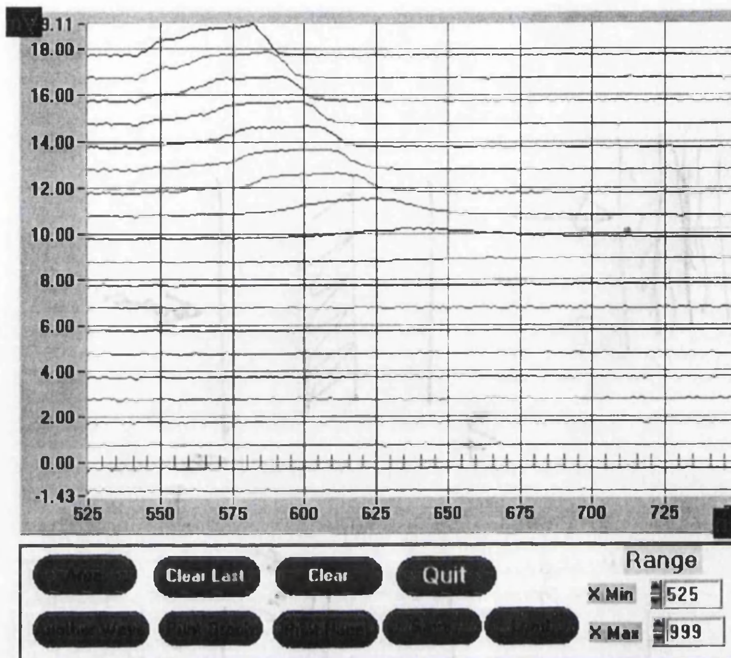

Figure 3.12: Sample B (SB) illuminated from n-side, hole drift.

both the surface and bulk. The microwaves have a wavelength of 3cm and enter orthogonal to the laser light pulses. The microwaves check the carrier concentration. As their frequency is fast, the carriers move in their field arround their locality. This process causes the absorption of microwave power but it does not redistribute the carriers. The period of microwaves is longer than the carrier scattering time and therefore the carrier is influenced by microwave electric field. However, the drift length is so small that it can be neglected. (If a higher power is applied then the drift could be comparable with the magnitude of micro-inhomogeneities and then the field from the microwaves could play a more important role) The devices used in this report typically had a mean carrier lifetime value of $\sim 40\mu s$ before irradiation, as shown in Figure 3.18. Non-irradiated silicon diodes have been compared

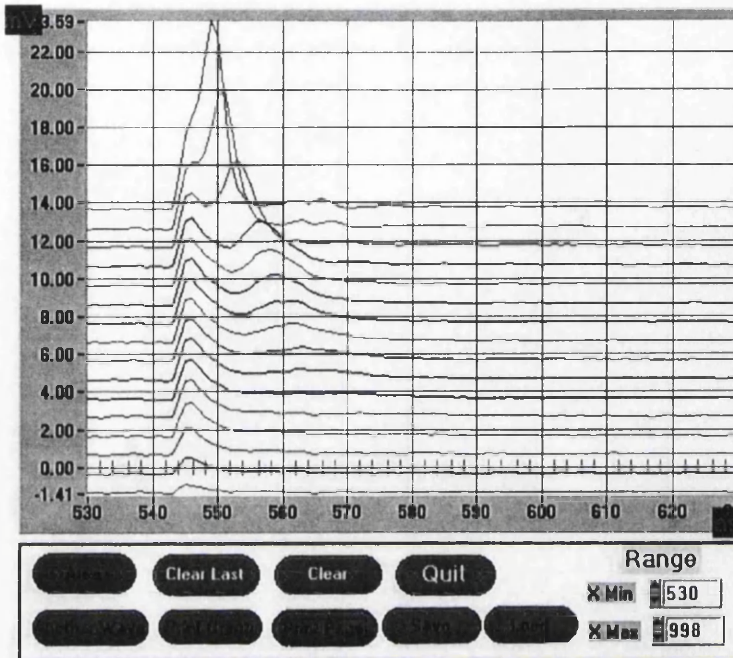

Figure 3.13: Sample C (SC) illuminated from the p-side.

with diodes irradiated with 450GeV Pb-ions. It is clear that the irradiated devices have greatly reduced excess carrier lifetimes due to the creation of radiation-induced defects that act as charge traps.

The longer the mean lifetime, the more chance a charge carrier will have of being collected. The drift time, τ, may be expressed as:

$$\tau = \frac{1}{N_T \sigma V_{th}} \tag{3.13}$$

where N_T is the trap concentration, σ the trap cross-section, and V_{th} the thermal velocity of the carrier. Again the importance of temperature is emphasised here. After being created, the particle drift time depends on its mobility, μ, and the electric field, E, applied across the device. The drift

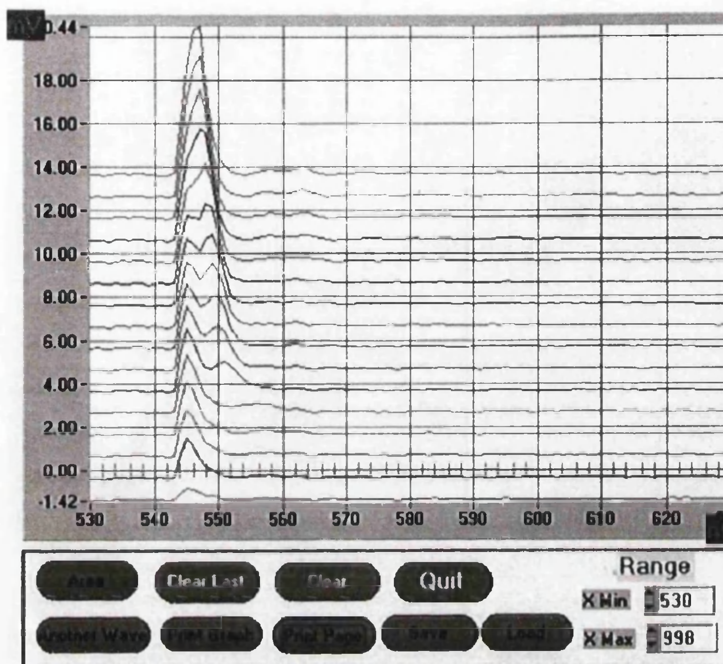

Figure 3.14: Sample D (SD) illuminated from the p-side.

length, L, may be expressed as:

$$L = \mu\tau E \tag{3.14}$$

These quantities determine the collected signal charge per unit drift length, Q, through the Hecht relation [12]:

$$Q = Q_0 exp(-\frac{x}{L}) \tag{3.15}$$

Excess carriers are generated by laser light of λ=1.1μm. Carrier transport is seen as current pulses recorded on a sampling oscilloscope. Assuming that

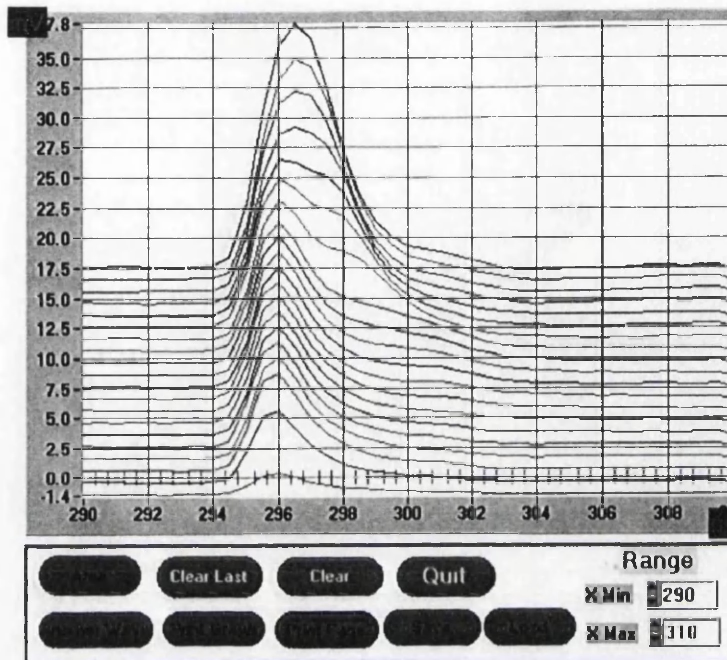

Figure 3.15: Sample E (SE) illumination from p-side.

at time t=0 there are n_0 carriers, and at time t there are n(t) carriers, one may write:

$$n(t) = n_0 exp(-\frac{t}{\tau}) \quad (3.16)$$

where t is the time of measurement and τ the carrier lifetime. The number of photons injected per second into the device, P, is controlled by the power of the laser, P_{opt}, given by:

$$P = \frac{P_{opt}}{h\nu} \quad (3.17)$$

At steady-state, carrier generation will equal carrier recombination. If

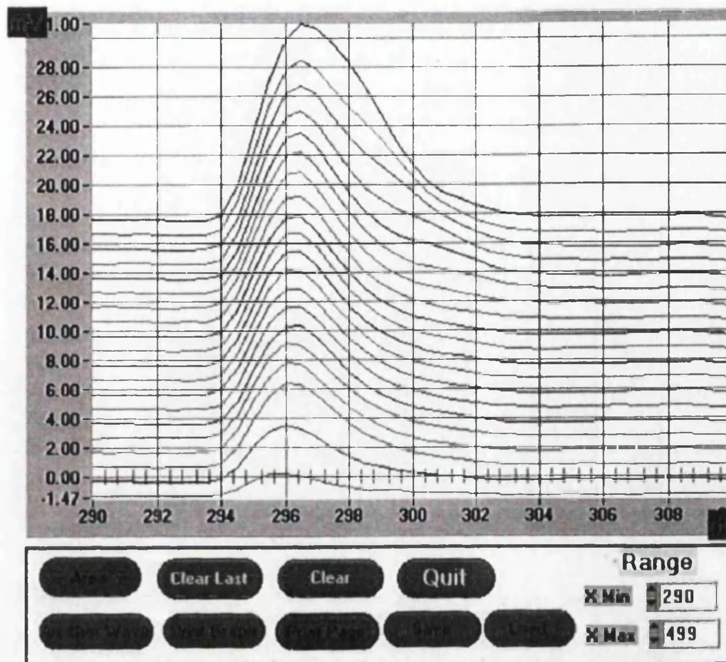

Figure 3.16: Sample F (SF) illuminated from p-side.

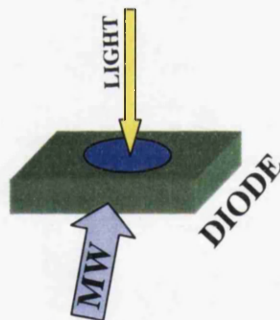

Figure 3.17: Schematic representation of the MWA technique experimental set-up showing a diode under illumination.

the diffusion length is very much greater than the mean light penetration depth $(1/\alpha)$, then the generation current, G, will be:

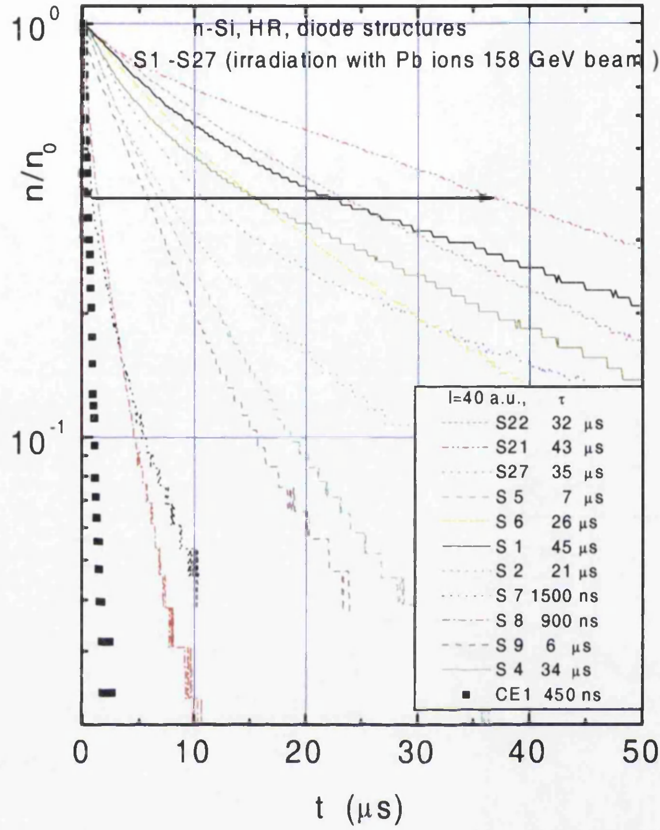

Figure 3.18: Excess carrier decay kinetics obtained on both irradiated and non-irradiated samples. Samples S21–S27 are non-irradiated diodes, while the others have various dose levels as documented in Table 3.2.

$$G = \frac{\eta}{WLD} \frac{P_{opt}}{h\nu} \tag{3.18}$$

where D is the diffussion constant, L the diffussion length, W the detector thickness and the quantum efficiency, η, is given by:

Relative Doses and Excess Carrier Lifetimes on Irradiated Diodes		
Sample name	Fluence (Pb/cm^2	Lifetime (μs)
S1	0	45
S5	6.5x10^9	7
S7	2.6x10^9	1.5
S8	4.8x10^{11}	0.96
S9	2.3x10^{10}	34
S21	0	43
S25	0	32
S27	0	35

Table 3.2: Irradiation fluence and carrier lifetime for each sample measured.

$$\eta = \frac{I_p}{q}\frac{h\nu}{P_{opt}} \tag{3.19}$$

where I_p is the photocurrent between the electrodes of the device. Combining these equations gives an expression for I_p:

$$I_p = q\frac{\eta P_{opt}}{h\nu}\frac{\mu\tau E}{L} \tag{3.20}$$

The response time is limited by the diffusion and drift time in the depletion zone. A caveat must be given concerning the capacitance in the depletion zone. If the depletion layer is too wide, then transit time effects limit the detector's response. If the depletion layer is very narrow, then the

excess capacitance will be dominant and only RC effects will be seen, which may lead to mis-interpretation of decay time for carrier lifetime. Ideally a depletion layer transit time is desired that is equal to about one half of the modulation period [52].

3.5 Summary

The various characterisation techniques described here are used extensively for irradiated and non-irradiated diodes. DLTS, while yielding important information regarding defect levels, does not give any indication of the electric field distribution in the device, unlike the TCT measurements. DLTS has been applied here to Pb-ion irradiated silicon samples and compared with proton, pion and neutron irradiation. The Pb-ions induce point like defect complexes and clustering. Applying TCT to proton irradiated silicon samples has shown the existence of a double junction beyond type inversion fluence. The MWA technique is a direct, non-destructive measurement of the excess carrier lifetime of a device. These techniques form an arsenal with which to assault the detector's surface and bulk to determine the causes of the deterioration of signal. Probing the Pb-ion irradiated samples has shown that the excess carrier lifetime is reduced dramatically with high fluence. However, all these techniques require charge carrier injection which alters N_{eff}. This effectively changes the charge in the space charge region. By flooding the device with carriers and observing their behaviour, one obtains a greater understanding of what is happening in the bulk but not how the device will behave under experimental conditions. Chapter 4 describes a technique for characterisation using X-ray photons that do not disrupt the

sign of the space charge region appreciably yet yield spectroscopic analysis of the entire bulk of the detector.

Chapter 4

Double Junction in Irradiated Silicon

4.1 *In Situ* Irradiation of Cryogenic Silicon

One of the aims of the RD39 Collaboration was to compare the irradiation of silicon detectors at room temperature with irradiation at cryogenic temperatures. The motivation for this measurement was to test the hypothesis that the Lazarus Effect may extend the lifetime of an irradiated device, and furthermore to show that irradiation at cryogenic temperatures would not be detrimental to detector performance. In what follows, a description is given of the author's contributions to these measurements, which included active participation in data-taking at the SPS, in particular assuming responsibility for monitoring of the devices during irradiation and analysis of test beam data that are presented here.

4.1.1 Experimental Set-up

A 400μm thick 3x3 silicon pad detector matrix was placed inside a liquid nitrogen (LN_2) continuous flow cryostat [53]. The active area of each pad was 1.5x1.5mm^2. Irradiation was carried out at the CERN-SPS, with a primary proton beam of 450GeV. The SPS delivers the beam to the test area in 14 second spills in which the beam lasts for a 2 second burst and the remaining 12 seconds are empty. As described below, the detector was irradiated and its response to MIPS measured *in situ* in order to provide measurements at ever increasing fluences. At each fluence, voltage scans and charge signal time dependence measurements were taken of the device being irradiated. The voltage was adjusted and the data were recorded at 3 minute intervals to observe how the charge collection efficiency changed with time. Between measurements the detector was left at 0V bias for stabilisation by filling of charge carrier traps. For the voltage scans, the beam intensity and energy were reduced by inserting a 5cm thick aluminium target at the proton beam focus 188m upstream from the detector, producing a 300GeV mixed proton and pion beam [54] with a Gaussian beam profile of transverse r.m.s., $\sigma_x \sim \sigma_y \sim$ 1mm. The beam was centred on the upper central pad of the 3x3 array and therefore the fluence on the irradiated pad can be considered uniform. The detector signal was read out using a charge amplifier (Amptek A225 [55]) placed outside the cryostat. The measured electronic noise of $\sim$ 2500 [43] electrons FWHM was dominated by the effect of the 30cm coaxial cable between the detector and the amplifier input. The signal was then fed into a sampling oscilloscope (LeCroy 9350) which built histograms of the charge spectrum. Detector leakage current and temperature were moni-

tored by a LabVIEW Slow Control software package, providing a warning of temperature increases over 2K.

4.1.2 Temperature Scan Results

In order to meet Goal 1 of the RD39 objectives, irradiation of a silicon detector was performed at both room temperature [41], and at liquid nitrogen temperature. Performing voltage scans at different temperatures gives some indications of relevant annealing effects, as illustrated in
Figure 4.1.

The scan at 83K before warming, Figure 4.1(a), shows that the CCE peaks around 67% at 200V bias following a fluence of $1.2\text{x}10^{15}\text{p/cm}^2$. For full depletion prior to irradiation, only 50V were required. At a fluence of $1.2\text{x}10^{15}\text{p/cm}^2$, the sample was annealed at 207K for 1 hour. From this beneficial annealing there is a marked improvement in CCE as shown in Figure 4.1(b). The detector was then cooled back down to 83K. The CCE again increased to 95% for 200V bias (Figure 4.1(c)). An interesting phenomenon is the signal time dependence [56]. At the lower fluence of $6.5\text{x}10^{14}\text{p/cm}^2$, the time dependence is not very pronounced. However, at the higher value of $1.2\text{x}10^{15}\text{p/cm}^2$ a stable value of the CCE is not reached until 15 minutes have passed, (Figure 4.1(d)).

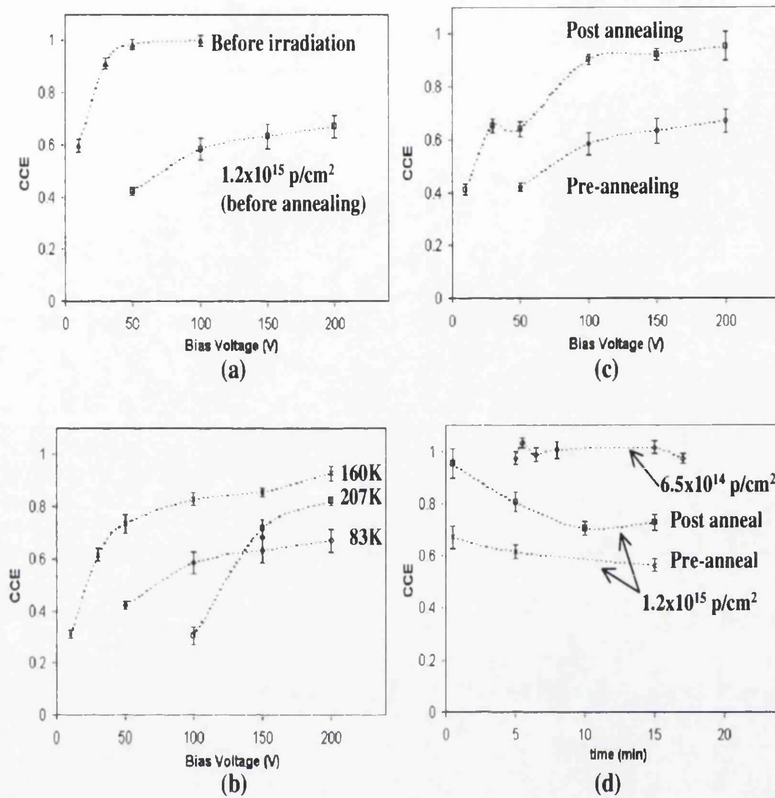

Figure 4.1: Graphs of the CCE.(a) Calibration curve with non-irradiated device and heavily irradiated device showing the CCE before annealing for 1 hour at 207K. (b) The CCE of the heavily irradiated sample taken as temperature is increased. (c) Comparison of the CCE of the heavily irradiated sample before and after warming. (d) Time dependence of the CCE is shown to be connected to the dose of irradiation.

4.1.3 Interpretation of the Results

Even after beneficial annealing, and the appliance of a high bias voltage, 100% CCE is not obtained. Cooling down to 130K gives the optimum conditions for minimum bias voltage with maximum active thickness, while re-

ducing the leakage current to negligible levels by freezing out traps. The problem is the change of N_{eff}. Irradiating beyond type inversion, N_{eff} becomes more and more positive. The highest electric field gradient is no longer at the p^+-side but instead is found at the n^+-side. Damage induced in the detector bulk by the irradiation prevents the field from being uniform across the device. As charge collected is given by Q.(d/D) (c.f. Equation 2.28), e-h pairs undergoing an intricate diffusion/drift motion, possibly involving trapping and de-trapping, will not contribute all of the charge deposited from an interaction in the detector medium on the electrode. In fact, the picture is more complicated since there will be a high field region at both front and back junctions dropping to a minimum in the damaged bulk. This "double junction" is discussed in detail below.

4.2 The Double Junction

The double junction has been observed previously in moderately irradiated semiconductors by the Lancaster group, (A. Chilingarov *et al.* [57]), following even earlier hints by Z. Li *et al.* [58]. Later results published by Z.Li and V. Eremin [59] used TCT experimental techniques to map out the electric field across silicon devices, showing the two high field regions. Complementary to this technique, X-ray absorption measurements were performed at Brunel University by S. Watts *et al.* [60]. Within the context of the RD39 Collaboration, a combination of measurements performed by the author at Brunel are discussed in detail in the following sections.

4.2.1 Experimental Set-up

The experimental results were obtained using the Brunel University system, shown schematically in figure 4.2.

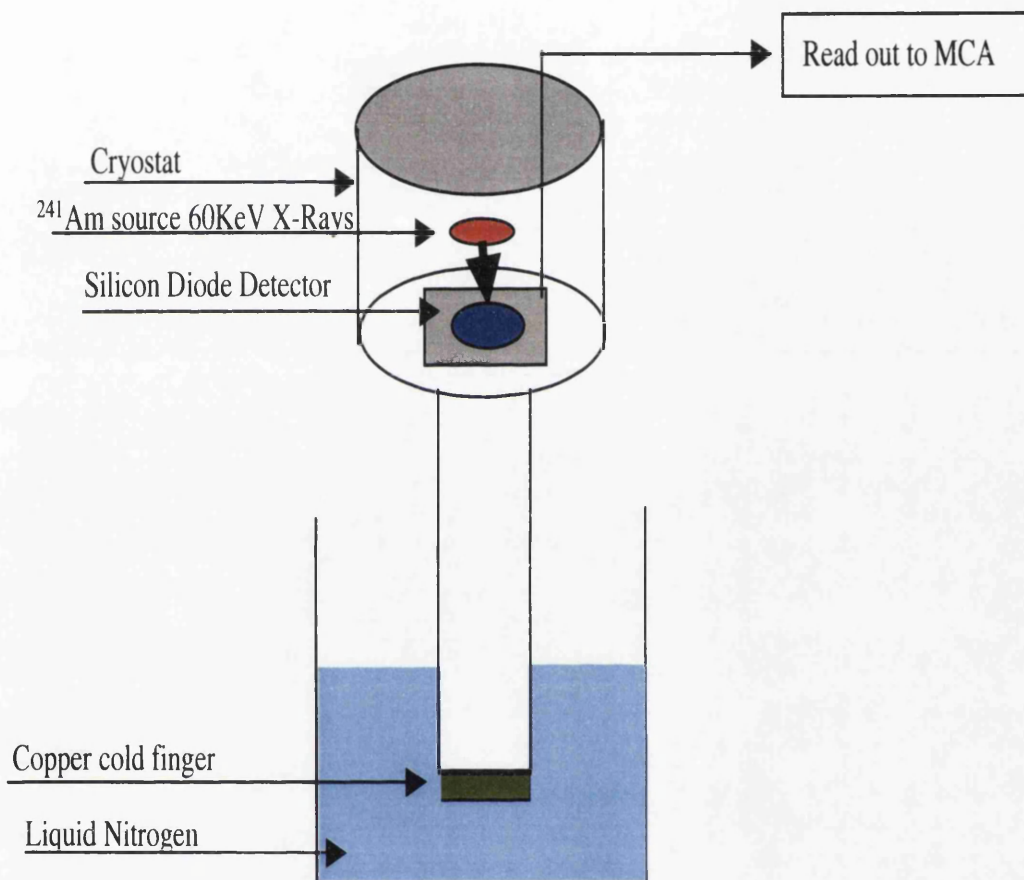

Figure 4.2: Schematic diagram of the cold finger cryostat used at Brunel to obtain results with X-ray sources on silicon devices.

The cryostat operates using the cold finger technique. This requires that the interior chamber, where samples are mounted, must be maintained under vacuum during running. The temperature of the sample was monitored using a thermistor diode, connected to a temperature gauge, and controlled

by varying the amount of insulation between the cold finger and the liquid nitrogen. It was thus possible to take measurements over a range of temperatures, maintaining a stable temperature for each measurement to within 2K. The radiation source was mounted over the sample, at a distance of (0.5$\pm$0.01)cm. The Americium-241 source used had a perspex sheet over the exit aperture to prevent the α-particles irradiating the sample. Only the 60keV γ-rays (and lower energy L-series X-rays, Table 2.1) from the source interacted with the detector. The source activity was 0.4μCi.

4.2.2 Calibration

Calibration of the set-up was performed using a non-irradiated 300μm silicon detector. This allows easy scaling to the 400μm irradiated silicon device. For the calibration curve, Americium-241 and Barium-133 spectra were recorded on the MCA. These two sources were used as they gave the "cleanest" signal. Figure 4.3 shows the pulse height distribution from the sources. Each source has characteristic energies as defined in Table 4.2.2.

Characteristic Energies of Calibration Sources	
Source	Energy (keV)
Barium	30, 36
Americium	60

Table 4.1: Energies emitted from sources used for calibration

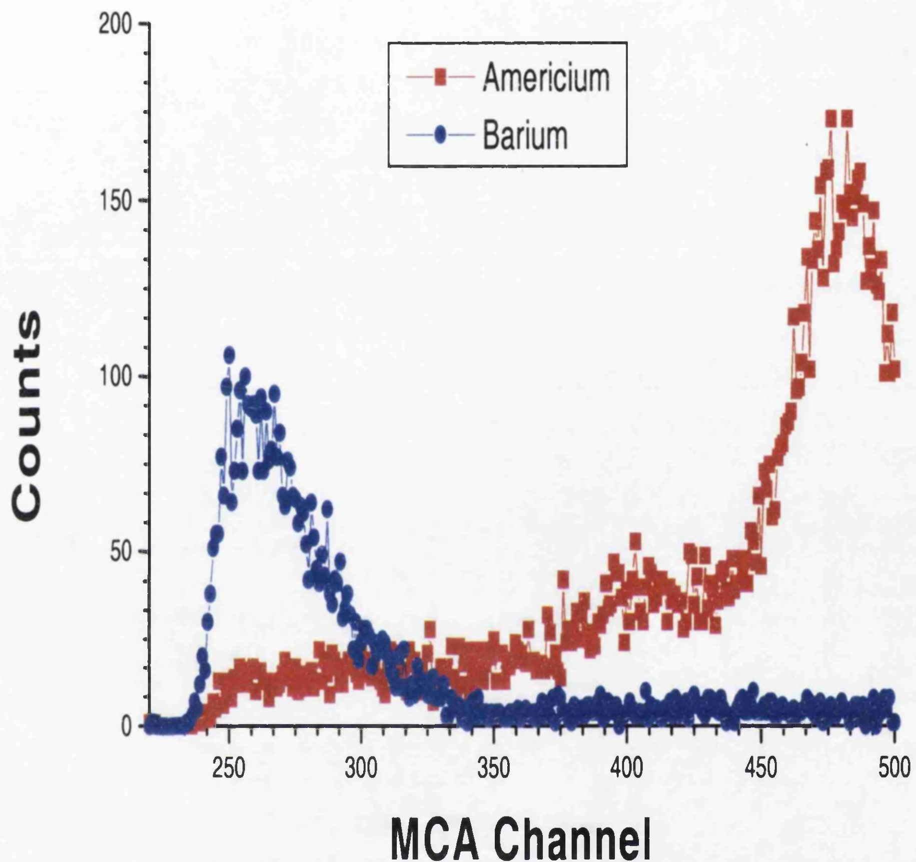

Figure 4.3: Graph showing Counts per channel vs. MCA Channel Number. Each channel corresponds to a particular energy, defined by the characteristic photo peak of each source.

4.2.3 Sample Preparation

The irradiated device to be tested was a 400μm thick, $p^+/n/n^+$ silicon detector fabricated at the Brookhaven National Laboratory, New York as described in Section 3.3.4. Irradiation was performed at the CERN PS facility

to $1x10^{14}cm^{-2}$ 1MeV neutron equivalent fluence. Before irradiation the detector had N_{eff}=$8.23x10^{11}cm^{-3}$ calculated using Equation 3.8.

As Figure 3.4 shows, as radiation dose increases, N_{eff} decreases to a minimum value. Beyond this "type inversion" point, N_{eff} increases linearly with 1MeV neutron equivalent fluence. As N_{eff} increases, the magnitude of voltage required for full depletion also increases linearly. The sample described here has been irradiated beyond type inversion, so the higher electric field region will be at the n^+ contact, as illustrated in Figure 4.5. By performing voltage scans at fixed temperatures and temperature scans at fixed voltages, one may examine different characteristics of the detector.

4.2.4 Analysis

The total flux of incident particles and the total number of X-rays absorbed by the detector may be calculated using:

$$N_{incident} = \frac{\text{Activity of source}}{4\pi r^2} \tag{4.1}$$

where r is the source-to-sample distance. This gives a flux of incident 60keV photons, $N_{incident}$, of (47.1±1.8)Mparticles/m^2/sec. The detector has an active area, A, of 5x5 mm^2. The number of particles absorbed per second, $N_{absorbed}$, is given by:

$$N_{absorbed} = (1 - exp[-\mu x]).N_{incident}.A \tag{4.2}$$

where μ is the linear absorption co-efficient of silicon for 60keV photons, and x the material thickness, in this case 300μm. Figure 4.4 shows that the absorption of 60keV X-rays in a 300μm thick silicon device for 60keV X-rays is essentially uniform throughout the bulk. As X-rays have an attenuation length of ~7cm [61][62] in silicon, the dose across the entire thickness of a 400μm silicon device will be comparable. This is of extreme importance for the examination of the entire detector bulk.

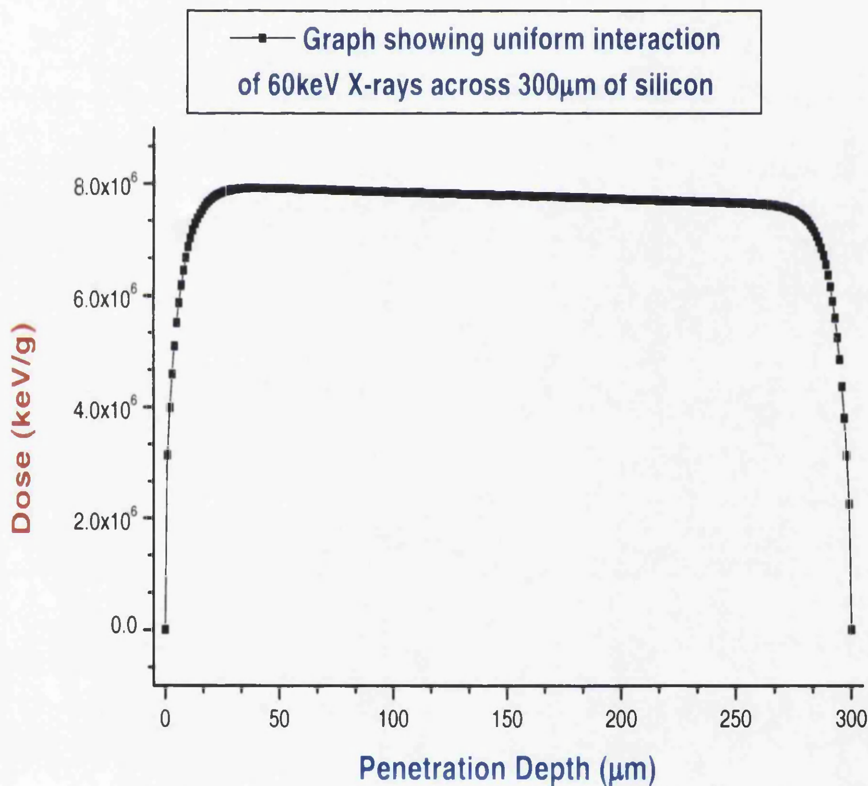

Figure 4.4: Graph showing penetration of 60keV X-rays into silicon. This was performed using Photcof (a 2D detector simulation software package).

At the point of photoelectric interaction of the photon, 60keV energy is released locally, creating around 16700 electron-hole pairs. Collection of the electrons and holes not only determines the charge collection efficiency of the device (from the response to individual photons), but can give the size of each depleted zone (from the measured intensity versus pulse height). For homogeneous interactions throughout the irradiated device, there are only three possible scenarios. A photon interacts either in the p^+ depleted zone, in the dead region between depleted zones, or in the n^+ depleted zone. Since output signal charge is only generated as the carriers move through an E-field, separate peaks are expected in the pulse height spectrum corresponding to X-ray absorption processes in each of these three regions. Interactions within a depleted zone will give a signal charge dependent upon how far the e-h pairs have travelled in the E-field. This is shown in Figure 4.5.

The count rate, the area under each peak in the pulse height spectrum, will give the thickness of the corresponding depleted zone. For the model shown in Figure 4.5 it is assumed that the contribution from the low field region is minimal. The implication of this is that 100% of the charge will never be collected, unless the strong fields overlap. This is verified experimentally in the results presented below.

4.2.5 Voltage Scans

Using the Americium-241 calibration source, voltage scans were performed over a range of temperatures from 207K down to 95K at intervals of $\sim$10K. The detector was maintained at each new temperature while the bias voltage was applied and data recorded over an acquisition time of 200s. As the de-

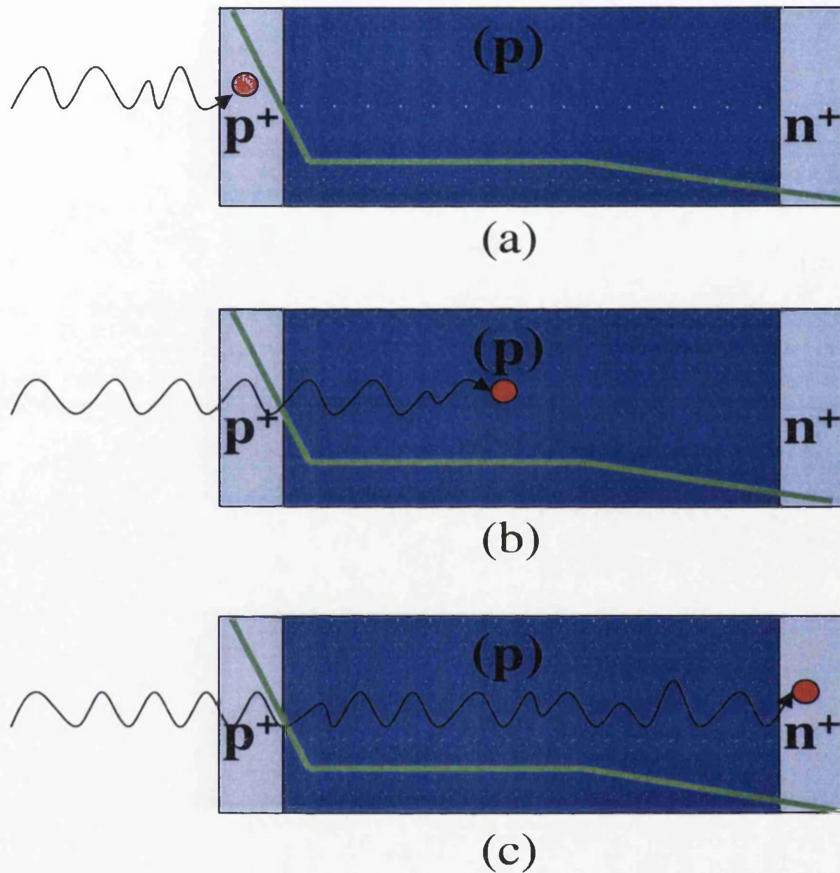

Figure 4.5: Possible X-ray interactions. (a) Photon interaction at the front depleted layer will give a signal contribution from the high E-field region. (b) In the "dead" low E-field region one assumes no, or very little, contribution to the collected signal charge. (c) Interaction in the back depleted region will also give a signal charge contribution due to the e-h movement in the high E-field.

tector was fully annealed, the CCE from signal charge are stable values and did not exhibit time dependence. Performing a voltage scan, while monitoring the MCA pulse height spectrum, one may observe the progression from under– to fully–depleted. Figure 4.6 shows the MCA photo peak position versus bias voltage.

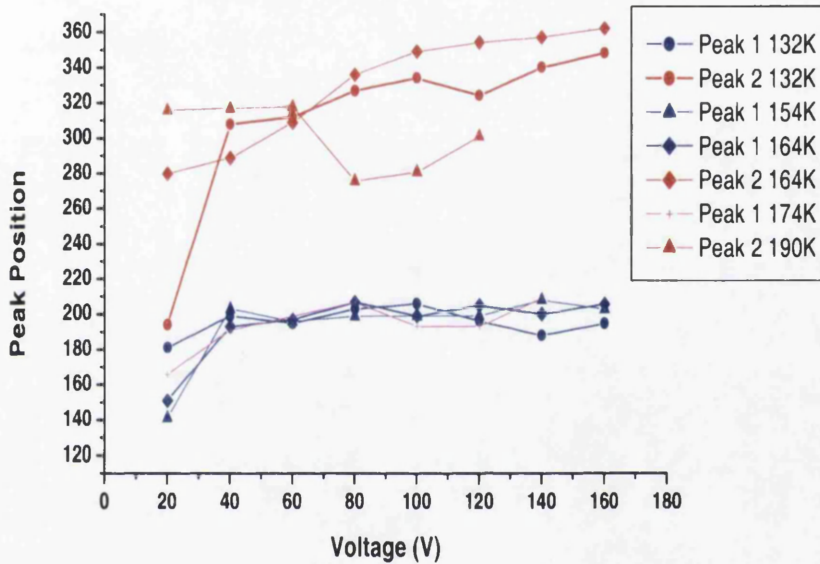

Figure 4.6: Multi-channel analyser data for temperature scans at 80V. Peak 1 corresponds to the electric field region near the P^+ contact. It is at a lower position, corresponding to less collected signal charge. Peak 2 corresponds to the higher position and higher collected charge peak. The signal collected is from the region near the n^+ contact with its higher electric field.

The lower energy peak maintains a constant position above 40V. This means essentially that a constant signal charge is being collected from this region and hence the depletion width from the p-side remains constant and the E-field may be considered unchanging in this region for decreasing tem-

perature and increasing voltage. The position of the higher energy peak, peak 2, tends to increase as the voltage is increased. A decrease in temperature reduces the noise, making the peaks more Gaussian. At 190K peak 2 is broadened due to the high radiation-induced leakage current and as a result the Gaussian fit is not as good resulting in loss of charge signal. As voltage is increased it follows the same trend as the other curves for 165K and 131K. This increasing trend implies that the detector is collecting more charge as the temperature is reduced and the depletion area increases. For 131K the CCE increase between 40V and 160V is about 5%. The E-field from the n-side is still extending as the voltage is increased. This will plateau as the damaged detector will not allow full depletion due to bulk changes. It has been shown recently that the E-field may be manipulated by local charge injection [40], hence dramatically altering N_{eff}, but this will not be discussed here.

4.2.6 Temperature Scans

Temperature scans were made while maintaining a constant voltage. The results exhibit Lazarus Effect characteristics, i.e. maximum depleted thickness for minimum bias voltage at 130K. A change in depletion thickness is observed as it is underdepleted at 80V. For temperatures above 200K, the results are dominated by noise from the radiation-induced damage increased leakage current. Below 200K, the charge signal emerges from the background. For 80V bias and below 200K, a peak at around channel 190 rises above the noise. Reducing the temperature further, to below 130K, a second peak can be seen around channel 320, (Figure 4.7).

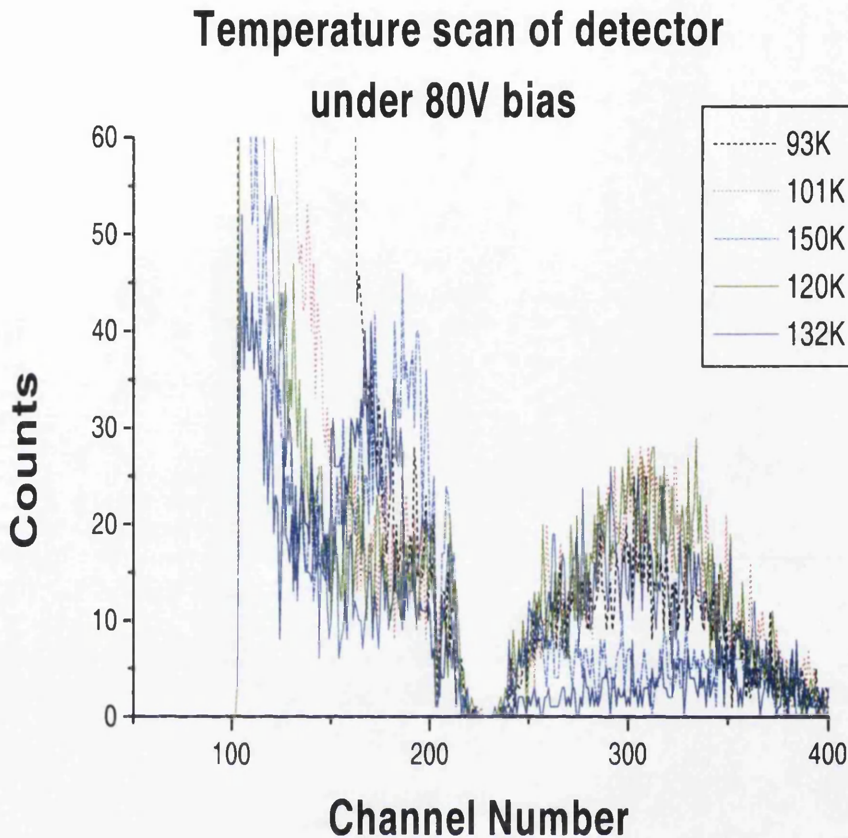

Figure 4.7: Multi-channel analyser data for temperature scans at 80V.

These two peaks in Figure 4.7 correspond to energies of 21keV and 38keV respectively. Considering the interaction probability of 60keV X-ray photons through 400μm silicon, one finds that there will be a uniform distribution of interactions across the bulk (Fig. 4.4). Taking this into account, it may be postulated that the two peaks are in fact are due to photons absorbed in the two depletion regions, at the front and back contacts respectively. The relative peak positions means that at 132K, and 80V bias, one depletion region is about twice the size of the other, assuming that the relative probabilities

of electron and hole trapping are the same in both depleted regions for the homogeneously irradiated device. However, the fact that the equivalent energies collected sum to give the total incident photon energy is not entirely unexpected due to the fact that the device is all but fully depleted. One can infer that there are two well defined strong field areas, but between them there must be either negligible dead space or a very weak interconnecting field. This may be checked by considering the count rate as discussed in Section 4.2.7.

4.2.7 Count Rate

Interpreting the count rate data, the area under the photo peak yields information on the size of the depletion area. Combining data from the voltage and temperature scans provides a collection of diagrams that act as "snapshots" in voltage and temperature for the depleted zone size, (Figure 4.8).

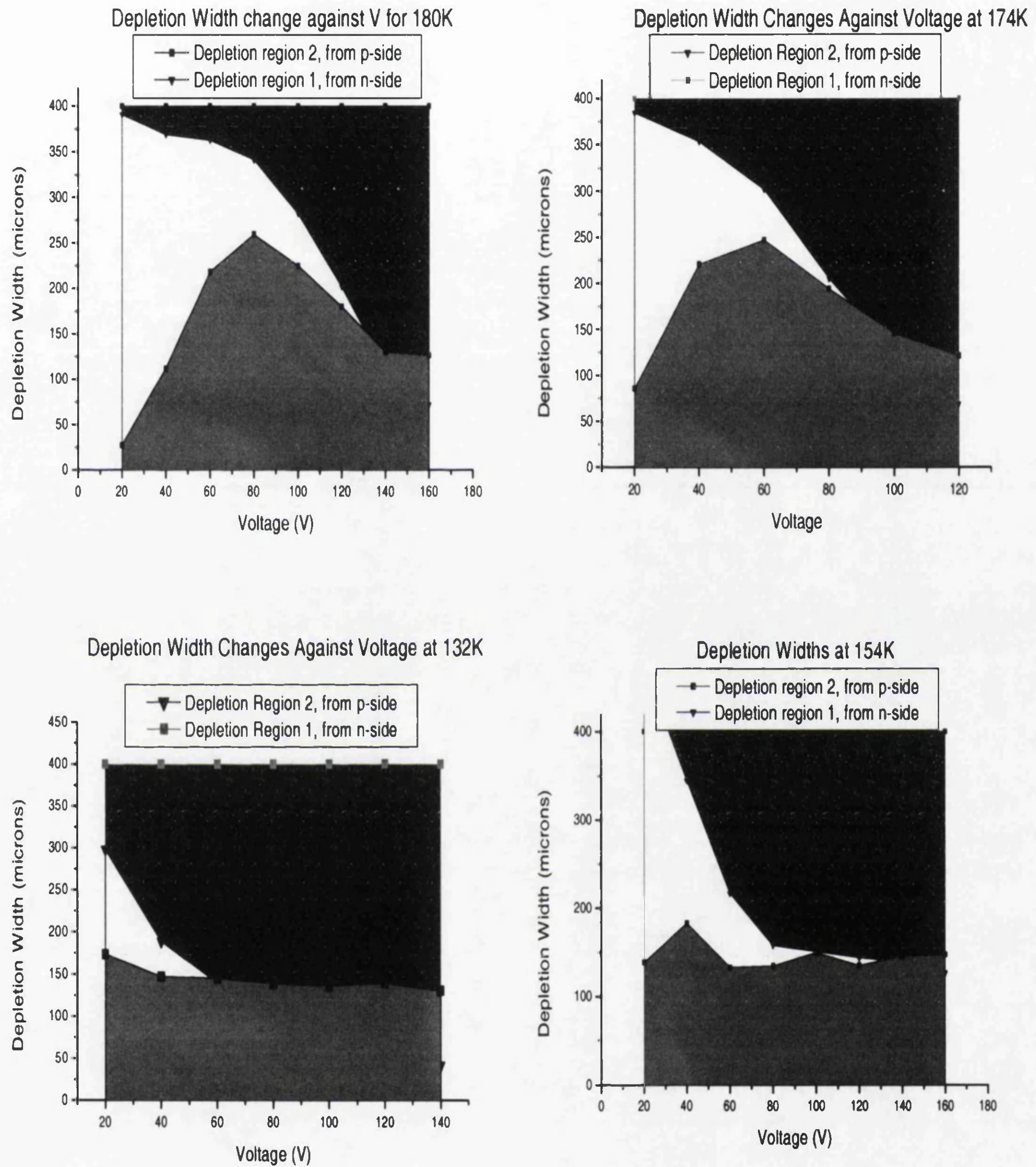

Figure 4.8: Depletion width sizes estimated from photo peak count rates.

Plotting detector sensitive thickness vs. voltage for specific temperatures allows easy identification of the progressive increase in depleted width as the temperature is reduced. An ~8% error arises from the fitting of the data, especially at higher temperatures, (T>170K), where noise levels are much higher, increasing the tail of the signal.

4.2.8 Discussion

As there are two high field regions, the device is behaving essentially as two p-n junctions.

The diffusion from the p^+-side has the effect only of reducing the p-n junction potential barrier at this point, hence reducing the field gradient at the p^+-side. At the n^+ contact the motion of carriers causes an enhancement of the junction barrier height and hence induces a higher electric field.

Results from TCT measurements (V. Eremin *et al.* [59]) show the existence of a double junction from the time dependence of the signal current pulse due to the drift of electrons or holes, depending on illumination of the p^+ contact or n^+ contact, respectively. Figure 4.9 shows TCT measurements made on a silicon sample irradiated beyond type inversion taken at Brookhaven National Laboratory[1].

The slope of the TCT pulse is an "image" of the electric field across the device [63]. From the bottom of Figure 4.9 to the top, the bias voltage across the device is incremented in regular steps. Initially there is one peak appearing at a lower energy, around channel 130, which corresponds to X-ray interactions in the lower E-field region from the p^+ contact. As the

[1]These data were taken by the author with Z. Li on a visit to BNL in December 2000.

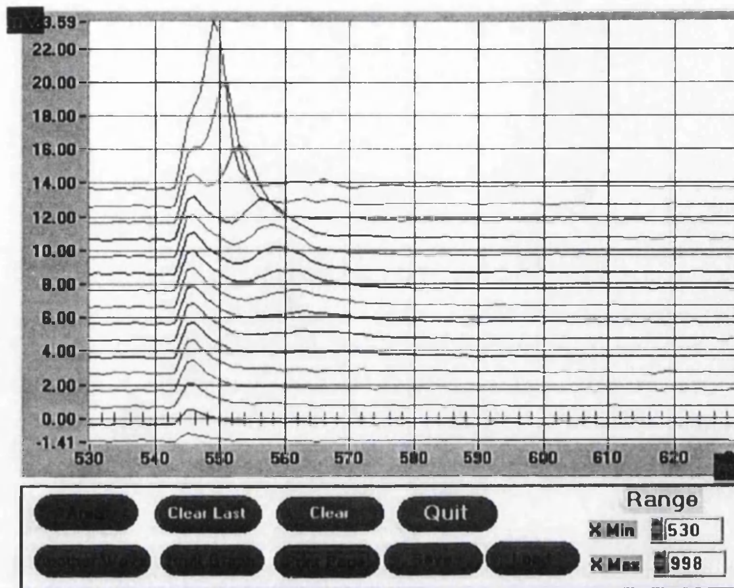

Figure 4.9: Measurements made at BNL.

voltage is increased the effect of an E-field from the n$^+$ contact becomes more apparent. By increasing the bias voltage the depletion area is increasing and the field extends further across the device. This is similar to decreasing the temperature in an under-depleted device. As temperature is decreased to 130K, the depletion area (for an under-depleted device) increases to a maximum. In the TCT measurements, as the bias increases further the second peak becomes more and more prominent and in fact larger than the initial peak observed. One can infer that the extending E-field from the n^+ contact is greater than that from the p$^+$ contact. Increasing the voltage further still leads to the two peaks merging by creating a single depletion area. Further studies using TCT provided examples of the effect of illumination of the p$^+$ and n$^+$ contacts, shown in Section 3.4.3. A difference in transient peak widths of a factor of 2 to 3 [64][65] for electron and hole drift, respectively,

is due to the difference in their mobilities.

The X-ray measurements are more subtle however. Wherever the photon interacts, it will deposit 60keV energy and since the charge collection efficiency depends on the field across the device, as well as charge trapping effects, one can consider the trapping probability, P_t:

$$P_t = \frac{\tau_{drift}}{\tau_{trap}} \tag{4.3}$$

Since the trapping time depends inversely on the thermal velocity, decreasing temperature increases the trapping time. This reduces the probability of trapping, as does a low drift time. For interactions close to the electrodes the electrons or holes will drift in a high field and deposit the signal charge fully on the electrodes. For the low field region, the carriers have a long way to drift and hence their probability of being trapped is greatly increased, reducing the amount of charge signal recorded from interactions in this area.

Chapter 5

Discussions

5.1 Conclusions and Future Experiments

It has been demonstrated that silicon semiconductor detectors irradiated at cryogenic temperatures perform as well as silicon devices irradiated at room temperature. Performing voltage scans on the irradiated detector pre- and post annealing, the charge collection efficiency was found to be 60% at 200V and 95% at 200V respectively. Time dependence measurements were presented, showing that for a fluence of 6.5×10^{14} p/cm^2 the time dependence of the charge collection efficiency is negligible. However, for the higher fluences of 1.2×10^{15} p/cm^2, the charge collection efficiency for reversed biased diodes will drop from an initial measured value of 67% to a stable value of 58% over a period of 15 minutes. Furthermore, silicon devices operated at cryogenic temperatures have the advantage of negligible radiation-induced leakage current (of the order of pA), allowing a cleaner signal to be measured by a charge sensitive amplifier. The cryogenic operation of silicon detectors offers an excellent opportunity for the LHC especially in the early stages for ac-

celerator beam monitoring [66] and leading proton measurements [67]. The RD39 Collaboration is working on the "Roman Pot" designs that will enable the silicon to be as close to the beam as possible while still maintaining signal integrity. By operating silicon detectors at 130K the voltage required for full depletion may be kept to a minimum. Furthermore, applying beneficial annealing to eliminate shallow radiation-induced defects, CCE may be optimised. Investigations are being performed on "edgeless devices". Various cleaving techniques are being explored that will allow specfic detector shapes and hence shroud the beam-pipe more effectively than square geometries. The relatively low cost of producing such $p^+/n/n^+$ detectors ensures that the replacement cost in event of failure would be minimal. For devices such as these, with $N_D \leq 10^{17}cm^{-3}$, the mobility of the carriers increases as temperature is reduced below 300K, increasing the operation speed of the devices [11].

DLTS measurements taken from Pb-ion irradiated silicon show the formation of point defect complexes unlike those identified in similar measurements made on equivalent detectors with proton, neutron and pion irradiation. The heavy ion project at CERN should work toward an appreciation of how one may relate heavy ion irradiation with previous reasonably well understood results from proton and neutron irradiation of silicon detectors.

Work funded by the Royal Society and co-ordinated by Glasgow and Vilnius will work toward *in situ* measurements on heavy ion irradiated silicon detectors to understand the mechanisms occurring inside the material during irradiation. Employing the microwave absorption technique one may analyse the carrier lifetimes as the device is irradiated. As shown for similar

devices, one may expect an average excess carrier lifetime of $\sim 38\mu s$ initially, while after irradiation this may be reduced to as little as a several hundred nanoseconds.

TCT measurements give very clean transient signals and yield much information regarding carrier mobilities and the E-field across a silicon detector. A modification of this technique would permit laser injection from the edge of a detector creating e-h pairs at specific positions across the detector thickness. Although, this would allow the examination of the E-field at precise positions across the device, it must be remembered that the injection of excess charge carriers via laser pulses alters the charge of the space charge region.

Employing the X-ray technique as described in Section 4.2.1, one may uniformly probe the bulk of a silicon detector without injecting excess carriers. An X-ray will deposit its energy locally where it interacts within the detector bulk. This technique has been shown to be powerful for uniform probing of the silicon detector bulk to allow an examination of the depletion widths after irradiation. As such it has led to this approach being adopted for testing devices in the basic research elements of the RD39 Collaboration.

Bibliography

[1] Beiser A. 1995 *Concepts of Modern Physics*, Fifth Ed. McGraw Hill.

[2] Blackey J. 1996 *Image Evaluation*, http://www.vdbs.com.

[3] Fernow F. 1986, *Radiation Detectors*, Cambridge University Press.

[4] Kennedy J. 2001, *The search for a light Higgs at LEP.* PhD Thesis, University of Glasgow, Scotland, G12 8QQ.

[5] ATLAS Collaboration 1999, *ATLAS Technical Design Report*, http://www.cern.ch/ATLAS.

[6] RD48 Collaboration, 2000 *3rd RD48 Status Report*, CERN/LHCC, 2000-009.

[7] Palmieri V.G.*et al.* 1998, *Cryogenic Operation of Silicon detectors: The Lazarus Effect*, Nuclear Instruments and Methods A 413:475.

[8] RD39 Collaboration Publications, 2000, *RD39 Collaboration Status Report* CERN/LHCC 2000-010, http://www.cern.ch/RD39/publications.

[9] Dearnaley G. 1963, *Radiation damage by charged particles in silicon junction detectors* IEEE Transactions on Nuclear Science, NS-10:106-110.

[10] RD48 Collaboration, 1998, *2nd RD48 Status Report*, CERN.

[11] Sze S.M. 1985, *Semiconductor Devices*, Wiley.

[12] Knoll G.F. 2000, *Radiation Detection and Measurement, Third Ed.*, Wiley.

[13] Ramo S. 1939, *Currents induced by electron motion*, P.I.R.E. 27:584-585.

[14] Cavalleri G., Fabri G., Gatti E. and Svelto V. 1963, *On induced charge in semiconductor detectors*, Nuclear Instruments and Methods 21:177-178.

[15] Cavalleri G., Gatti E. 1971, *Extensions of Ramo's theorem as applied to induced charge in semiconductor detectors*, Nuclear Instruments and Methods 92:137-140.

[16] Martini M., Ottaviani G. 1969, *Ramo's theorem and the energy balance equations in evaluating the current pulse from semiconductor detectors*, Nuclear Instruments and Methods 67:177-178.

[17] Kim H. 1991. *An extended proof of the Ramo-Shockley theorem*, Solid State Electronics, Vol. 34, No. 11:1251-1253.

[18] Passmore S. 2001, *Pixel Detectors*, PhD Thesis, University of Glasgow, Scotland, G12 8QQ.

[19] Toussignat O., Hamel L.A. and Vasilevki D. 1998, *Weighting potentials in CdZnTe γ-ray detectors with segmented electrodes*, IEEE NSS Toronto.

[20] NIST. 2000, *Stopping power and range tables for alpha particles*, http://physics.nist.gov/cgi–bin/Star/ap_table.pl

[21] Bates R. 1997, *Gallium Arsenide Radiation Detectors for the ATLAS Experiment*, PhD Thesis, University of Glasgow, G12 8QQ, Scotland.

[22] Skyrme D.J. 1967, Nuclear Instruments and Methods, 57:61.

[23] http://physics.nist.gov/PhysRefData.

[24] Alberigi Quaranta A., Martini M. and Ottaviani G. 1968, *The pulse shape and the timing problem in solid state detectors*, Manuscript received by NSG.

[25] Ortec 2001, *Amplifiers*, http://www.ortec-online.com

[26] Da Via C. 2000, *RD39 Collaboration Meeting*, http://www.cern.ch/RD39.

[27] RD48 Collaboration, 2001, *RD48 Collaboration Homepage*, http://www.cern.ch/RD48.

[28] Lazo M.S., Woodall D.M. and McDaniel P.J. 1987, *Silicon and silicon dioxide neutron damage functions*, In Proc. Fast Burt React. Workshop, Sandia National Lab., SAND87-0098, Vol.1:85-103.

[29] RD39 Collaboration, 2001, *RD39 Collaboration Homepage*, http://www.cern.ch/RD39.

[30] Griffen P. *et al.* 1996, *Neutron cross-sections taken from ENDF/B-VI, ORNL*, unpublished but available from G. Lindstrom, Hamburg.

[31] Konobeyev A.Yu. *et al.* 1992, *Neutron displacement cross-sections for structural materials below 800MeV*, J. Nuclear Mater, 186:117.

[32] Summers G.P. *et al.* 1993 *Damage correlations in semiconductors to gamma, electron and proton radiations*, IEEE Transactions on Nuclear Science, NS-40:1372.

[33] Huhtinen M. and Aarino P.A. 1993, *Estimation of pion induced displacement damage in silicon*, HU-SEFT R, 1993-02.

[34] Huhtinen M. and Aarino P.A. 1993, *Pion induced displacement damage in silicon devices*, Nuclear Instruments and Methods in Physics Research, A:335-580.

[35] Lutz G. 1999, *Semiconductor radiation detectors*, Springer.

[36] Eremin V., Li Z. and Iljashenko I. 1995, *Trapping induced N_{eff} and electrical field transformation at different temperatures in neutron irradiated high resistivity silicon detectors*, N.I.M. A 360:458-462.

[37] Borchi E. and Bruzzi M. 1994, *Radiataion damage in silicon detectors*, Rivista del Nuovo Cimento, Vol. 17, N. 11.

[38] Pintilie I. 2000, *Comparison between microscopic damages induced by neutron and proton irradiation in silicon detectors*, 2nd ENDEASD Workshop Proceedings, Editor Claeys C.

[39] Moll M. 1999 *Radiation Damage in Silicon Particle Detectors*, PhD Thesis, University of Hamburg.

[40] Verbitskaya E. *et al.* 2001, *Optimisation of electric field distribution by free carrier injection in silicon detectors operated at low temperatures*, RD39 Collaboration to be published in NIM A.

[41] Collins P. *et al.* 2000, *Charge collection efficiency and resolution of an irradiated double-sided silicon microstrip detector operated at cryogenic temperatures*, Nuclear Instruments and Methods, A440:17-37.

[42] Ruggiero G. 1999, *Resistenza alla radiazione di rivelatori al silico operanti a temperature criogeniche*, Universita degli studi di Napoli "Federico II", Tesi di laurea in fisica.

[43] Eremin V., Bohm J., Roe S., Ruggiero G., and Weilhammer P. *The charge collection in single side silicon microstrip detectors*, to be published in NIM A.

[44] Palmieri V. *et al.* 1998, *Experimental test of the hybrid superconducting detector principle*, Nuclear Instruments and Methods A 417:111-123.

[45] Polaron Equipment Ltd. *DL 4600 DLTS System Instruction Manual*, Bio-rad.

[46] Kuhnke M., Fretwurst E. and Lindstroem G. 2001, *Microscopic studies on various silicon materials irradiated with different high energetic particles*, 2nd ENDEASD Workshop, Kista, Sweden.

[47] Trauwaert M.A. 1995, *Radiation and impurity related deep levels in Si: a DLTS study correlated with other spectroscopic techniques.*, PhD thesis, Leuven.

[48] Devine S. and Gaubas E. *Investigations on Pb-ion irradiation of silicon devices*, to be published in NIM A.

[49] Gaubas E. and Vanhellemont J. 1996, *A simple technique for the separation of bulk and surface recombination parameters in silicon*, Journal of Applied Physics. 80(11):6293-6297.

[50] Gaubas E. *et al.* 1997, *Investigation of recombination parameters in silicon structures by infared and microwave transient absorption technique.*, Semiconductor Science and Technology, 12:1-10.

[51] Li Z. 2000, *Private communication*, Brookhaven National Laboratory, New York, USA.

[52] Gaubas E. *et al.* 1997, *Study of recombination properties of neutron transmutation doped silicon wafers*, Semicond. Sci. Technol. 12:1092-1097.

[53] Ruggiero G. *et al.* 2000, *Silicon detectors irradiated "in situ" at cryogenic temperatures*, to be published in Nuclear Instruments and Methods A.

[54] Sonderegger P. 1999, *Private communication.*

[55] Amptek, http://www.amptek.com

[56] Borer K. *et al.* 2000, *Charge collection efficiency of irradiated silicon detector operated at cryogenic temperature*, Nuclear Instruments and Methods, A440:5-16.

[57] Chilingarov A. *et al.* 1998, *Electric field in irradiated silicon detectors*, Nuclear Instruments and Methods, A418:314-321.

[58] Li Z. and Kraner H.W. 1992, Journal of Electron. Mater. 21:701.

[59] Menichelli D., Bruzzi M., Li Z., and Eremin V. 1999, *Modelling of observed double-junction*, Nuclear Instruments and Methods A426:135-139.

[60] Da Via C., Watts S. and Devine S. *X-ray examination of the double junction effect.*, to be published in NIM A.

[61] 1998 *Review of Particle Physics*, The European Physical Journal C, Volume 3, Number 1-4.

[62] Dargys A. and Kundrotas J. 1994, *Handbook on Physical Properties of Ge, Si, GaAs and InP*, Science and Encyclopedia Publishers.

[63] Li Z. 2000, *Private communications.*

[64] Canali C. *et al.* 1975, *Electron drift velocity in silicon*, Physical Review B, Vol. 12, 6:2265-2268.

[65] Ottaviani G. *et al.*, 1975 *Hole drift velocity in silicon*, Physical Review Vol. 12, 8:3318-3329.

[66] *Proposal to extend ATLAS for luminosity measurements and forward physics* Draft 0.1 for internal use only.

[67] Totem Collaboration, 1999, *Total cross section, elastic scattering and diffraction dissociation at the LHC*, CERN/LHC 99-7.